UNIVERSIDADE DA BEIRA INTERIOR
Engenharia

Hydrodynamic Optimization of a torpedo-shaped hull

Tiago Correia Bartolomeu

Dissertação para a obtenção do Grau de Mestre em
Engenharia Aeronáutica
(Ciclo de estudos integrado)

Orientadores: Ph.D. Francisco Miguel Ribeiro Proença Brójo
M.Sc. Paulo de Vasconcelos Figueiredo

Covilhã, outubro de 2016

Acknowledgments

There are many people whom I would like to thank for helping me over the last six months. To them, I am sincerely grateful.

Firstly, I would like to express my deepest gratitude to my supervisor at UBI, Professor Francisco Brójo, whom was always there for me, making this thesis possible. I am truly thankful for the given opportunity to work with CEiiA. You were always helpful, providing me the essential lessons, especially on the laboratory. Further, I always felt welcomed and comfortable under your guidance.

Further, my gratitude goes to my supervisor at CEiiA, Paulo Figueiredo. You always dedicated your time helping me, indicating me the right path to follow. I have greatly appreciated your support. Thank you for everything.

At the same time, I would like to thank CEiiA for the given opportunity. It was an amazing experience, reaching me as person and future professional. Moreover, this gratitude obviously includes CEiiA's team: Tiago Rebelo, David Brandão and Flávio Raimundo. I have no words to describe your kindness and everything you have done to help me finish this thesis.

I would also like to thank to the three laboratory technicians, Mr. Rui Paulo, Mr. Jorge Barros and Mr. João Correia, for all the support that you have given me during the experimental setup.

Thank you all whom helped me during this thesis, especially a huge thanks to my friends Cláudio, Rafael, Flávio, Luís, Marcos, Thiago, Afonso, Salvador, Samuel, André, José, Tiago, Filipe, Nuno and Hugo. More than helping me, you are always there for me.

Finally, I would like to thank all of my family for their unconditional love. Everything I am today, was tailored from your support. I am forever thankful to my parents, Maria and Vitor, for providing me the opportunity to get this far. To my sister, Rita, there are no words to describe everything you have done for me. I am forever grateful for your love and understanding.

Dedication

This M. Sc. Thesis is dedicated to the two women of my life…

… to my beloved Mother, Maria José de Oliveira Correia

… to my dear Sister, Rita Correia Bartolomeu

"*If not us, who? If not now, when?*"

- John F. Kennedy

Resumo

Hoje em dia, não é ainda completamente claro de que maneira o fundo dos oceanos podem contribuir para os Ecossistemas da Terra. Contudo, vários esforços estão a ser feito para compreender em profundidade os fundos marinhos dos Oceanos. Atualmente, o método mais eficiente, já desenvolvido, para explorar a profundeza dos oceanos é conhecido como veículos submarinos, e especificamente, o mais eficiente para pesquisa e exploração destes é conhecido como Veículo Autónomo Subaquático (AUV). O aumento do uso de AUV's tem levado a um ponto em que os parâmetros de projeto são cruciais. Características como a resistência ao avanço, o alto tempo de operação, a grande manobrabilidade e o grande alcance são exigidos numa fase primária de projeto; desta forma, é fundamental encontrar uma forma ótima do corpo hidrodinâmico, ainda durante a fase de projeto, ambicionando melhorar as suas características. Esta dissertação apresenta o efeito das forças hidrodinâmicas de veículos subaquáticos axi-simétricos através da variação da forma de um corpo em forma de torpedo. Além disso, nesta dissertação pretende-se ainda analisar, experimentalmente, os rácios comprimento/diâmetro do nariz e da cauda do corpo, assim como as suas formas, para que seja possível os rácios e combinação ótimos do ponto de vista da minimização da resistência ao avanço. Os testes experimentais foram feitos num tanque de água da Universidade da Beira Interior (UBI). No entanto, devido às dimensões do tanque de água, o desenvolvimento de um modelo à escala foi a opção mais viável. Uma similaridade entre o modelo à escala e o protótipo foi feita para garantir as mesmas condições de escoamento entre ambos. Várias combinações foram testadas experimentalmente e seguidamente validadas por simulações numéricas. Adicionalmente, parâmetros como o ângulo de ataque (de 0 - 20˚) e a velocidade (entre 0.50 – 1 m/s) foram alterados para perceber a sua influência na resistência hidrodinâmica. A preparação experimental é totalmente descrita, mostrando vários procedimentos adotados até à fase de recolha de dados. Um sistema de tensão/compressão (célula de carga) foi utilizado para medir a resistência induzido pelo corpo. Os resultados experimentais demonstraram uma configuração ótima que se situa nas proximidades de N/D = 0.8 (Forma Elítica) e T/D = 1.6 (Forma Cónica). Pode ser visto que a resistência aumenta com o aumento da velocidade. Da mesma forma para os ângulos de ataque, a resistência aumenta para ângulos de ataque maiores. Os dados experimentais foram usados para validar os resultados obtidos de um software CFD que usa as equações RANS. Um estudo de independência da malha foi feito para investigar dois modelos turbulentos: Modelos Standard κ-ε e κ-ω SST. O modelo turbulento Standard κ-ε mostrou ser o mais apropriado para este estudo com um menor custo computacional. Os resultados entre os métodos experimentais e numéricos mostraram uma boa concordância, considerando as condições mencionadas.

Palavras-chave

Veículo Autónomo Subaquático (*AUV*), força de resistência ao avanço, Dinâmica de Fluídos Computacional (CFD), totalmente submerso, *hull body*, Nariz, Cauda, Modelos Turbulentos.

Abstract

Nowadays, it is not fully clear how the Ocean seabed can contribute to Earth ecosystems. However, several steps are being taken to completely understand Ocean's seabed. Lately, many methods are being developed to explore the Oceans, although there is one method which fulfill the desired trade-off (between low operational costs and high quality data collection). This efficient method developed to explore the Ocean's depth is known as submarine vehicles, and the most efficient of them, to explore and mapping, is certainly the Autonomous Underwater Vehicle (AUV). The increasing use of AUV's is leading to a point in which its design parameters are crucial. Characteristics as high endurance, long operation time, high maneuverability and range are demanded at an early design stage; thus, it is essential to find an optimum hull shape design to improve these characteristics. This thesis presents the effect of hydrodynamic forces of axisymmetric underwater vehicles through the variation of the shape of a torpedo-shaped hull body. Furthermore, this thesis is intended to analyze, experimentally, the length-to-Diameter (D) ratios of nose (N) and tail (T), as well as its shapes, in order to find the optimum ratios and shape combinations for the minimization of Drag. The experimental tests were conducted in the towing tank of the University of Beira Interior (UBI). However, due to the Towing Tank dimensions, the development of a scaled model had to be made. A similarity between the scaled model and the full-scale prototype must be done to assume similar flow conditions. Several torpedo-shaped combinations were tested experimentally and further validated the numerical simulations. Moreover, parameters such as the pitch angles (or Angle of Attack (AoA)) [0 - 20°] and velocities [0.50 – 1 m/s] were investigated to understand their influence on the hydrodynamic Drag. The experimental setup is hereby fully described, showing the various procedures adopted until the data collection phase. A strain gauge system (load cell) was used to measure the Drag induced by the hull body. Experimental results demonstrate an optimum configuration for N/D = 0.8 (Elliptical shape) and T/D = 1.6 (Conical shape). From the experimental and numerical data, it could be seen that the Drag increases with the increase of velocity. Same occurrence happens for AoA, where Drag increases with higher AoA's. Therefore, it can be concluded that the influence of AoA on Drag is higher for greater velocities. The experimental measurements have been used to validate results obtained from a Computational Fluid Dynamics (CFD) software that uses Reynolds Average Navier-Stokes (RANS) equations (ANSYS™ FLUENT). A mesh-independency study was made to investigate two turbulence models: Standard κ-ε and κ-ω SST models. Standard κ-ε showed to be the most appropriate model to this study with a lower computational cost. Results between Experimental and Numerical methods showed a good agreement, considering the conditions mentioned.

Keywords

Autonomous Underwater Vehicle (AUV), Drag (D_T), Computational Fluid Dynamics (CFD), fully submerged, hull body, Nose, Tail, Turbulence Models.

Contents

List of Figures

List of Tables

List of Charts

List of Acronyms

ABE	Autonomous Benthic Explorer
AGAVE	Artics GAkkel Vents Expedition
AKN	Abe-Nagano-Kondoh
AoA	Angle of attack
ASE	Analytical and Semi-Empirical
ASV	Autonomous Surface Vehicle
ASW	Anti-Submarine Warfare
AUG	Autonomous Underwater Glider
AUSS	Advanced Unmanned Search System
AUV	Autonomous Underwater Vehicle
CAD	Computer-Aided Design
CEiiA	Centre of Engineering and Product Development
CFD	Computational Fluid Dynamics
CN3	Communications/Navigation Network Node
CNC	Computer Numeric Control
CV	Control Volume
DNS	Direct Numerical Simulation
EMEPC	Estrutura de Missão para a Extensão da Plataforma Continental
FFI	Norwegian Defence Research Establishment
HOV	Human Occupied Vehicle
IFREMER	French Research Institute for Exploitation of the Sea
IMAR	Institute of Marine Research
IMPA, IP	The Portuguese Sea and Atmosphere Institute, I.P.
ISR	Instituto de Sistemas e Robótica
IST	Instituto Superior Técnico
ITTC	International Towing Tank Conference
LARS	Launch And Recovery System
LES	Large Eddy Simulation
MARINET	Marine Renewables Infrastructure Networks
MCM	Mine CounterMeasures
MIG	Metal Inert Gas
MIT	Massachusetts Institute of Technology
PC	Personal Computer
PIV	Particle Image Velocimetry
RANS	Reynolds Averaged Navier-Stokes
REMUS	Remote Environmental Monitoring UnitS
RNG	Renormalization-group
ROV	Remotely Operated Vehicle
RSM	Reynolds Stress Model
SLS	Selective Laser Sintering
SPAWAR	Space and Naval Warfare Systems Command
SPURV	Special Purpose Underwater Research Vehicle
SST	Shear-Stress Transport
UBI	University of Beira Interior

USA	United States of America
UUST	Unmanned Untethered Submersible Technology
UUV	Unmanned Underwater Vehicle
WB	WorkBench
WHOI	Woods Hole Oceanographic Institution
WWII	Word War Two

Nomenclature

B	Buoyancy	[N]
Bl	Blockage Ratio	[-]
C_D	Drag coefficient	[-]
C_F	Friction Resistance Coefficient	[-]
C_P	Prismatic Coefficient	[-]
C_R	Residual Drag Coefficient	[-]
D	Diameter	[mm]
d	Distance	[m]
D_T	Drag	[N]
Fn	Froude Number	[-]
F_R	Resistance Force	[N]
g	Acceleration due to Gravity	[m/s^2]
h	Submergence depth	[mm]
H^*	Submergence depth-to-diameter Ratio	[-]
K	Thermal conductivity coefficient	[-]
L	Length	[mm]
l	Characteristic Linear Dimension	[m]
m	Mass	[g]
p	Pressure	[Pa]
q	Fluid Velocity Vector	[m/s]
Re	Reynolds Number	[-]
S	Wetted Surface Area	[m^2]
S_O	Maximum Cross Sectional area of the Towing Tank	[m^2]
t	Time	[s]
U	Velocity	[m/s]
V	Volume	[m^3]

Greek letters

y	Distance of the first layer of the cells to the hull	[mm]
y^+	Distance from body's surface to the near wall node	[-]
α	Maximum Cross Sectional area of the Model	[m^2]
γ	Specific Heats Ratio	[-]
δ_{ij}	Kronecker delta function	[-]
ε	Turbulence Dissipation Rate	[m^2/s^3]
κ	Turbulence Kinetic Energy	[m^2/s^2]
μ	Absolute Viscosity	[kg/(s.m)]
μ^*	Friction velocity	[m/s]
ν	Kinematic Viscosity	[kg/(s.m)]
ρ	Density	[kg/m^3]
τ_W	Shear Stress	[N/m^2]
ω	Specific Dissipation Rate	[m^2/s^3]
∇	Volume of the envelope	[m^3]

Chapter 1

1 Introduction

1.1 Motivation

Oceans are a significant component of the Earth's surface forming the majority of the hydrosphere. It is certain that the ocean covers more than 2/3 of the Earth's surface, being a fundamental reason of human's existence on Earth. Moreover, the average depth of the ocean is 3680 meters and the greatest ocean depth of the oceans is found in Mariana's trench, with 10911 m depth. However, only about 5% of the oceans bottoms have been explored [1]. Therefore, it is extremely important to explore as much as possible this unknown area and understand how oceans can improve human lives. The collection of ocean data by observation and tracking in actual sea is crucial.

In order to understand the ocean, several tools have been used in the offshore industry since the late 1960s. These tools must comply with certain characteristics to carry out their functions [2]. Lately, tools as Human Occupied Vehicles (HOV's), Remotely Operated Vehicles (ROV's) and Autonomous Underwater Vehicles (AUV's) are being used for an extensive and complex study of the oceans, revolutionizing the process of gathering ocean data [1], [3]. However, the relative high cost of using instruments lowered from research ships (HOV's) or tethered robots (ROV's) and their limitations such as the need for a communications tether or an operating vessel have limited their use. Consequently, AUV's became a common tool in ocean sampling by being independent, and are now an indispensable feature for collecting ocean data providing a safe, cost-effective and reliable alternative to manned or remotely controlled systems [4]-[7].

In recent years, AUV's are becoming a powerful tool in deep ocean research, being increasingly used in areas such as, the exploration of underwater environments, maintenance and repair of submerged structures, mineral exploration, military use, pipeline inspection, mine-sweeping and many other areas [8], [9]. These several distinct applications give rise to a large number of different vehicle shapes and sizes. The design of AUV's is conducted by a demanding tradeoff between the crucial requirements of the missions, and the main constraints of fabrication, assembly and operational logistics. However, an AUV is limited when power requirements are concerned, which directly impacts its characteristics, such as velocity, range and endurance of the vehicle [6], [10]. Thus, it is crucial to find an efficient hydrodynamic design that reduce power consumption, and in turn, increase AUV's autonomy. In order to improve its performance on a design project level, the reduction of hull's hydrodynamic resistance must be the main

focus. Therefore, an increasing use of AUV's leads the need to investigate and predict, efficiently, the hydrodynamic forces acting over an AUV [11].

This research thesis further analyzes, through the use of experimental and numerical methods, the hydrodynamic forces and coefficients of an AUV with a torpedo shape operating under deeply submerged conditions. The AUV model velocity, Angle of Attack (AoA), Nose Length / Diameter and Tail Length / Diameter ratios are investigated to study their effect on hydrodynamics performance of submerged vehicles. For this purpose, a detailed experimental procedure has to be performed by a numerical study using a commercial Computational Fluid Dynamics (CFD) tool, FLUENT ANSYS 16.0., being the ultimate goal of this thesis the validation of the numerical simulation against the experimental procedure, allowing for the optimization of the overall AUV body.

1.2 Research Objectives and Aim

CEiia - the Centre of Engineering and Product Development challenged the author of this thesis to study, experimentally and numerically, the hydrodynamic forces and coefficients of an AUV model based on MEDUSA DEEP-SEA AUV type. MEDUSA Deep-Sea AUV is a double-hull design that is currently being developed by a group of partners: CEiiA, Instituto de Sistemas e Robótica (ISR) from Instituto Superior Técnico (IST), The Portuguese Sea and Atmosphere Institute, I.P. (IPMA, IP), EMEPC (Estrutura de Missão para a Extensão da Plataforma Continental) (governmental structure with a mission to prepare/monitor the process of extending the continental shelf of Portugal), Institute of Marine Research (IMAR) and Argus Remote Systems AS. This project embraces the design and production of a specific AUV for the required conditions imposed initially to operate at 3000 m of depth and with a specific payload. More details about this project are shown in reference [12]. Vehicle's configuration is shown in Figure 1.1. This thesis is not a part of MEDUSA Deep-Sea project, being rather considered a parallel study which might help optimize this vehicle's hydrodynamic hull efficiency.

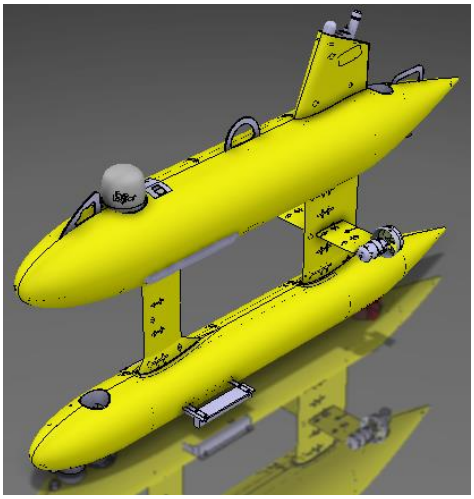

Figure 1.1 – MEDUSA Deep-Sea Conceptual Design.

The following objectives were defined for this research:

- Investigate the effects of velocity, AoA, Nose/Diameter and Tail/Diameter ratios on the hydrodynamic forces and coefficients generated by an AUV hull form operating in a fully submerged depth condition;
- Implement the experimental procedure to investigate the hydrodynamic forces and coefficients;
- Investigate the application of CFD numerical methods for predicting underwater vehicle's hydrodynamic coefficients;
- Validate the numerical simulation process against the experimental testing results;
- Identify optimum configurations and conditions for AUV's taking into consideration vehicle's velocity, AoA, Nose/Diameter and Tail/Diameter ratios.

The aim of this project is to validate the numerical simulation against the experimental procedure (see Figure 1.2). For this purpose, the towing tank of UBI shall be set properly to do the experiments and experimental data should be collected. The CFD tool shall be used to obtain numerical data to achieve the proposed objectives.

1.3 Research Strategy and Document Structure

The research strategy undertaken in this project comprises the use of the following three interrelated research tools:

- Investigation through an extensive literature review to report on the relevant work completed by other authors, and support the experiment and numerical based investigations;
- Investigation by experiment to observe, measure and register the hydrodynamic forces and calculate coefficients through data collected, of a fully submerged AUV hull form;
- Investigate, implement, analyze and evaluate a CFD numerical simulation to predict the resistance force and drag coefficient experienced by a fully submerged AUV model.

This document is structured in a coherent and logical manner. The description of each chapter within this document is presented below:

Chapter 1 introduces the motivation to the research problem, presents its aim and the research objectives expected to be achieved during this study.

Chapter 2 provides a literature review of Unmanned Underwater Vehicles (UUV's), the hydrodynamic phenomena environment of a submerged AUV body and the relevant experimental and numerical research completed to date by other authors.

Chapter 3 describes the specific case study of this thesis, as well as its requirements and parameters that are aimed to be studied.

Chapter 4 presents the experimental procedure, including the experimental model design and its manufacturing, and experimental setup, used to calculate the forces of the AUV model operating without free surface and wall effect. It also presents the results of the experimental tests.

Chapter 5 discusses the CFD software used to simulate and predict the hydrodynamic forces and coefficients of the AUV model, assuming fully submerged depth condition. It also provides the modelling and simulation methods adopted in this research, as well as its results.

Chapter 6 presents the conclusions drawn from the experimental procedure and numerical simulation, the difficulties encountered during this thesis, and the areas which need further investigation.

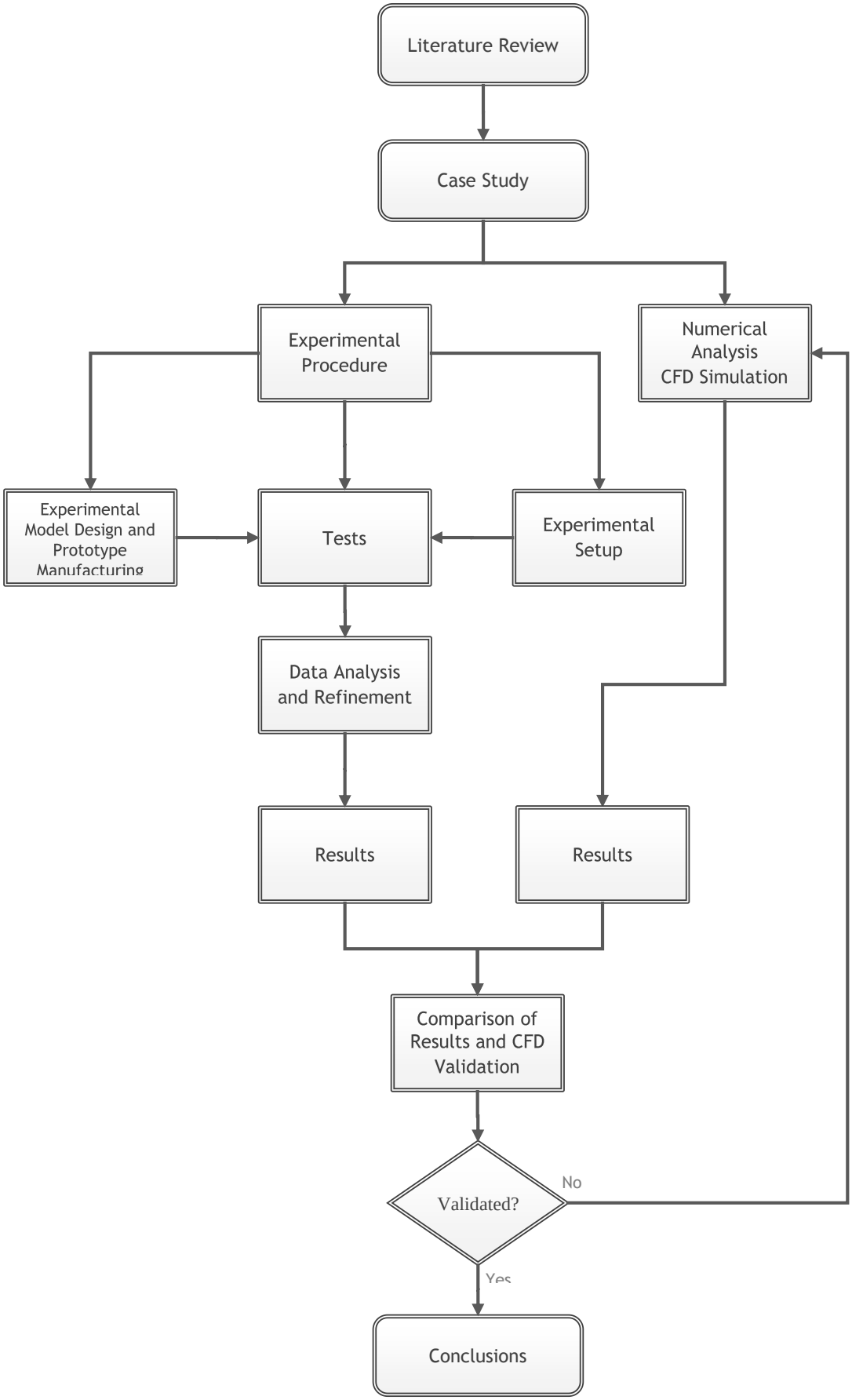

Figure 1.2 - Thesis structure flow diagram.

Chapter 2

2 Literature Review and Significant Theory

It is essential to understand background knowledge and fundamental milestones about the AUV history, as well as, similar studies made by other authors. It is also important to understand the reasons for the underwater vehicle's shape at different phases of their development and some notable achievements.

2.1 History

AUV's are directly linked to streamlined bodies, being the majority torpedo-shaped. The first torpedo was invented by Robert Whitehead in Austria in 1866 [13], [14], but this concept only started being dominant and reliable since World War II (WWII) [15]. The name Torpedo came from the Torpedo fish, which is an electric ray capable of delivering a stunning shock to its prey. The torpedo can be considered the first AUV, if the fact that it carried an explosive payload is ignored. Furthermore, this torpedo achieved a speed of 3 m/s and ran around 700 m [16]. The torpedo-shaped is a crucial parameter for this study because it is straightly connected with actual AUV's design.

The development of UUV's started in the 1960's and some initial research was made about the utility of UUV's. The first successful one was developed as early as 1957 in the Applied Physics Laboratory at the University of Washington to gather data from the Arctic regions. This UUV was named as the Special Purpose Underwater Research Vehicle (SPURV I) and was subject of study until the mid 70's. Between the 70's and 80's the SPURV II was adopted, an upgrade more capable than SPURV I. Altogether were released over 400 SPURV [16], [17]. Table 2.1 shows some of SPURV I's specifications.

Table 2.1 - SPURV I Specifications (adapted from [18]).

Maximum Depth	3600 [m]
Endurance with LR 90 battery	5.5 hours (hr)
Instrument Payload	45 [kg]
Speed	2-2.5 [m/s]
Displacement (sea water)	430 [kg]
Net Buoyancy	9.1 [kg]
Overall Length	3.1 [m]
Diameter	0.508 [m]
Dive Rate	1.3 [m/s]
Climb Rate	2.3 [m/s]
Turn Rate	3 [°/s]
Acoustic Tracking Range	2000 [m]

In 1973, the Naval Ocean System Center, now known as Space and Naval Warfare Systems Command (SPAWAR) started to develop the Advanced Unmanned Search System (AUSS). This vehicle was ready for the first launch ten years later, in 1983. Had a displacement of 907 kg, with 5,2 m long and 0,8 m of diameter, completed over 114 dives being some of them to 6000 m of depth [5], [16].

In 1976, the French Research Institute for Exploitation of the Sea (IFREMER) designed Epulard vehicle. This vehicle was assembled by 1978 and was operational for the first dive in 1980. It had a maximum depth of 6000 m and was acoustically controlled, Epulard completed about 300 dives between 1970 and 1990 [16].

During the 70's, other AUV's were also developed at the Massachusetts Institute of Technology (MIT). Later, in 1997, a group of engineers from the MIT AUV Laboratory founded BLUEFIN ROBOTICS. This company develops, builds, and operates AUV's and related technologies. Recently, was acquired by General Dynamics Mission Systems, a business unit of General Dynamics [19].

In 1980, the "International Symposium on Unmanned Untethered Submersible Technology" (UUST) was created in Durham, New Hampshire, United States of America (USA), with twenty-four technologist attending this conference. Seven years later, more than 320 people were representing more than 100 companies, 20 Universities and 20 federal agencies on the meeting [17].

During the 80's, there were many technological advances apart from AUV community that critically improved AUV development. Improvements like software systems and size reduction of hardware systems were crucial. Following Busby's 1987 Undersea Vehicle Directory, there were six operational AUV's and other 15 vehicles considered prototypes or under construction by 1987 [5], [16].

In 1990, the HUGIN AUV program started in a project between KONGSBERG and the Norwegian Defence Research Establishment (FFI). Since its development has been the most capable and successful commercial AUV in operation. Figure 2.1 shows the HUGIN AUV Product Range and their specifications [20], [21].

	HUGIN 1000	HUGIN 1000 for 3000 m	HUGIN 3000	HUGIN 4500
Weight	650-850 kg	650-850 kg	1400 kg	1900 kg
Length	4.5 m	4.7 m	5.5 m	6.0 m
Diameter	0.75 m	0.75 m	1.00 m	1.00 m
Speed	2-6 kts	2-6 kts	2-4 kts	2-4 kts
Depth	1000 m	3000 m	3000 m	4500 m
Battery	LiPolymer pressure tolerant. 15 KWh	LiPolymer pressure tolerant. 15 KWh	Al/HP semi fuel cell, 45 KWh	Al/HP semi fuel cell, 60 KWh
Endurance	24hrs @ 4kts (with MBE, SSS, SBP and CTD)	24hrs @ 4kts (with MBE, SSS, SBP and CTD)	60hrs @ 4kts (with MBE, SSS, SBP and CTD)	60hrs @ 4kts (with MBE, SSS, SBP and CTD)
Navigation system and sensors (main + options)	NavP AINS: IMU, DVL, Depth, USBL, NavP TP Ranging, GPS, TerrNav	NavP AINS: IMU, DVL, Depth, USBL, NavP TP Ranging, GPS, TerrNav	NavP AINS: IMU, DVL, Depth, USBL, NavP TP Ranging, GPS, TerrNav	NavP AINS: IMU, DVL, Depth, USBL, NavP TP Ranging, GPS, TerrNav
Communication (main + options)	Acoustic command and data links, RF, Iridium, Ethernet, WLAN	Acoustic command and data links, RF, Iridium, Ethernet, WLAN	Acoustic command and data links, RF, Iridium, Ethernet, WLAN	Acoustic command and data links, RF, Iridium, Ethernet, WLAN
Payloads (main + options)	MBE, SSS, SBP, SAS, CTD turbidity sonsor, ADCP, camera+ others	MBE, SSS, SBP, CTD turbidity sonsor, ADCP, camera + others	MBE, SSS, SBP, CTD ADCP, camera + others	MBE, SSS, SBP, CTD, ADCP + others
Main applications	Naval, research, offshore, hydrography	Naval, research, offshore, hydrograpy	Offshore, research	Offshore, research

Figure 2.1 – Specifications of several HUGIN AUV's [20].

In the 90's, the first generation of operational systems able to be tasked to perform defined objectives appeared, in other words, AUV's grew from proof of concept to a final result. Therewith, the interest in AUV's academic research increased quickly.

During the 90's, the Massachusetts Institute of Technology's Sea Grand AUV lab developed six Odyssey vehicles. These vehicles had a displacement of 160 kg, with an operational speed of

1.5 m/s, operating for up to six hours and were assigned to 6000 m of depth. In 1994, these vehicles operated under ice, and in 1995 operated for 3 hours in the open ocean to a depth of 1400 m [16], [17].

Almost at the same time, in the early 90's, the Woods Hole Oceanographic Institute (WHOI) developed the Autonomous Benthic Explorer (ABE) (see Figure 2.2). ABE completed its first scientific mission in 1994, had a displacement of 680 kg and its dives typically lasted about 16 to 34 hours depending on the instrument payload and bottom terrain. This vehicle was the first one to be completely independent of the surface vessel and capable of covering large areas of underwater terrain. ABE was extremely maneuverable due to its six thrusters. Its deepest dive to date was 4000 m, in its at least 80 dives [5], [16]. Figure 2.2 demonstrates ABE AUV attached to the Launch And Recovering System (LARS).

Figure 2.2 – ABE AUV during a mission (adapted from [1]).

At the same time, the South Hampton Oceanography Center's AUTOSUB was developed. AUTOSUB was the first vehicle prepared for long duration missions, having completed its first scientific mission in 1998. With a travelling speed of 1.5 m/s, it displaces 1700 kg and can operate for up to six days. This vehicle has completed over 270 missions covering more than 3500 km. Its longest mission lasted 50 hours [5], [16].

In the late 90's, WHOI's Remote Environmental Monitoring UnitS (REMUS) vehicle was developed in the Oceanographic Systems Lab (now marketed by Hydroid, owned by Kongsberg Group in 2007) to support scientific objectives at the LEO-15 observatory in Tuckerton, New Jersey. Its first scientific mission was in 1997 and there are currently over 50 REMUS vehicles in 20 different configurations that are being independently operated by universities and agencies, so it is not possible to determine how many missions have been performed by REMUS. With a displacement of 36 kg, it can operate for up to 20 hours at 1.5 m/s and to a depth of 100 m.

Its longest mission lasted 17 hours, with an operational speed of 1.75 m/s at a maximum depth of 20 m of the coast of New Jersey [1], [16]. The Figure 2.3 shows a recent version of a REMUS AUV, the REMUS 6000. This vehicle can operate in water depths up to 6000 m and its autonomy depend on its speed/sensor configuration (typical mission duration is 22 hr).

Figure 2.3 – REMUS 6000 operating near free surface (adapted from [22]).

In 1997, the HUGIN I AUV made the first commercial survey operation for the Ásgard Gas Transport Pipeline Route. This is an important milestone for the AUV civilian application. This survey confirmed the expected improvements in efficiency and data quality by the use of AUV's. From 2001, these vehicles have been successfully used for military application [20].

In 2004 the Navy UUV Master Plan was issued. This plan defines UUV missions in the following prioritized order [23]:

1. Intelligence, Surveillance, and Reconnaissance;
2. Mine Countermeasures (MCM);
3. Anti-Submarine Warfare (ASW);
4. Inspection/Identification;
5. Oceanography;
6. Communications/Navigation Network Node (CN3);
7. Payload Delivery.

This UUV Master Plan is a document recommending AUV missions and technologies.

Since the beginning of this century, it became clear that the use of AUV technology was of great value for several commercial tasks. There is a transitioning point in which AUV technology will definitely move from the research environment into the commercial offshore industry. Although, there are some parameters to be performed, such as the economic viability of the

technology and some technological problems, to continue its advance for industry to embrace its potential.

Currently, there are many companies on the AUV industry such as Kongsberg Maritime (owner of the most-known brands as REMUS, HUGIN, MUNIN or SEAGLIDER), BLUEFIN ROBOTICS or International Submarine Engineering. These companies are being constantly supported by research institutions as WHOI, MIT AUV Laboratory or Kongsberg Group (two centuries business company, owner of Kongsberg Maritime) to expand this industry.

2.2 Unmanned Underwater Vehicles (UUV's)

Since the main topic of this thesis is AUV's, it is not relevant to have an exhaustive study about all marine vehicles. However, it is extremely important to understand their global classification like it is shown in Figure 2.4.

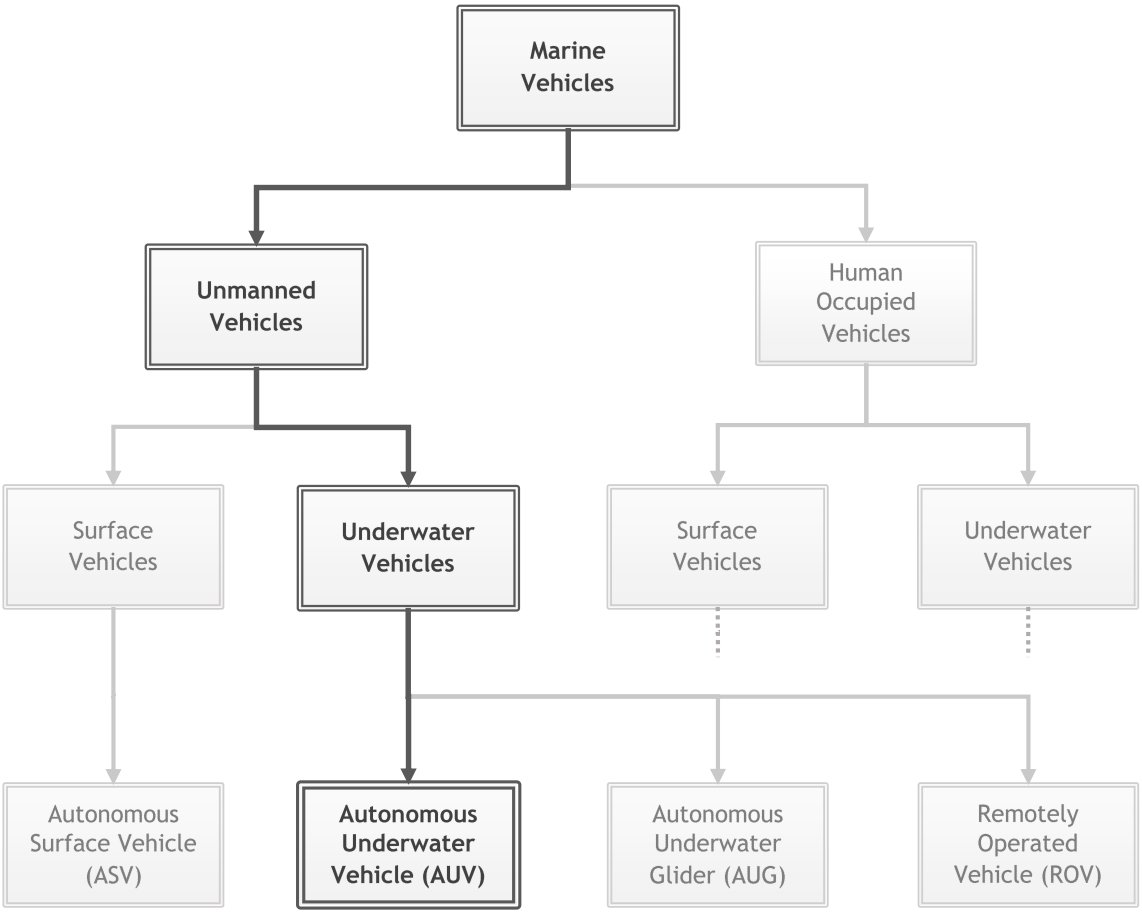

Figure 2.4 - Global classification of marine vehicles.

Unmanned Vehicles can be described by dividing them into two categories: Underwater Vehicles and Surface Vehicles.

The Unmanned Surface Vehicles, most known as Autonomous Surface Vehicles (ASV's) are vehicles that only operate in the ocean's surface. Depending on its vessel, length and power supply, they can operate for a considerable time (weeks or months).

The Unmanned Underwater Vehicles (UUV's) are mainly separated into three categories: Remotely Operated Vehicle (ROV), Autonomous Underwater Vehicle (AUV) and Autonomous Underwater Glider (AUG). Depending on each specific task, the type of UUV should be chosen properly. However, characteristics such as high endurance, long operation time, high maneuverability and range are always desired. The relationships between those four characteristics are shown in Figure 2.5.

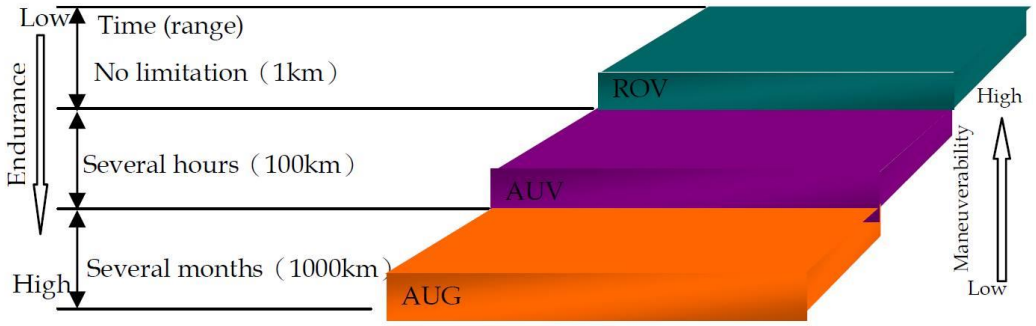

Figure 2.5 - Relationship between Endurance, Time, Range and Maneuverability (adapted from [4]).

2.3 Autonomous Underwater Vehicles – Design and Concepts

The design of an AUV depends on its mission and in a preliminary design concept it is highly important to understand which geometry/shape is better for the desired mission.

Nowadays, with the development of technology came the increase in the use of AUV's. Mainly, there are three different types of applications for AUV's:

- Commercial: directly linked with oil and gas industries; its traditional missions are the mapping and tracking of the seafloor before construct any infrastructure, also pipelines can be monitored easily.
- Defense: obviously connected with defense or protection; this AUV application involve missions as mine detection, monitoring an area to identify unknown objects and detection of manned submarines (anti-submarine warfare).
- Research: this is the pioneer application, came with the necessity to know the ocean's life and study precisely new elements attached to the sea floor.

Depending on each mission, there are several variables that can be changed during the preliminary design such as, for example, the AUV Length (L) and/or Diameter (D).

2.4 General Design of an AUV

There are some aspects in AUV design that need special attention, and are known as major design aspects. These aspects include: hull design, propulsion, submerging and electric power [2]. Therefore, these aspects can be subdivided into several subsystems as [23]:

- the pressure container;
- the hydrodynamic hull;
- ballasting;
- power and energy;
- electrical-power distribution;
- propulsion;
- navigation and positioning;
- obstacle avoidance;
- masts;
- maneuver control;
- communications;
- locator and emergency equipment;
- payloads.

Since the aim of this thesis is to estimate/calculate the hydrodynamic forces/coefficients, it is crucial to improve backgrounds in hull design, and specifically in hydrodynamic hull. For a detailed study about the subsystems please refer to the references [2], [23].

2.4.1 Hydrodynamic Design

An AUV when travelling through the ocean should be highly hydrodynamic or as much as possible streamlined. Frequently, the components housing defines several restrictions as minimum Diameter (cross-sectional area) or Length, and these restrictions directly affect the body's hydrodynamic. Reduce Drag (D_T), or also known as Resistance Force (F_R), is always one of the main design objectives. Moreover, the flow over an AUV's body should be controlled for an efficient propulsion i.e. laminar flow designs should be chosen [23]. Maximum cross section from nose and nose/tail radius (same length with different curvature) are parameters that also have influence on resistance force, but since they are not controllable due to the constraints of this study, will be neglected. The F_R depends on a set of phenomena as can be shown in Figure 2.6.

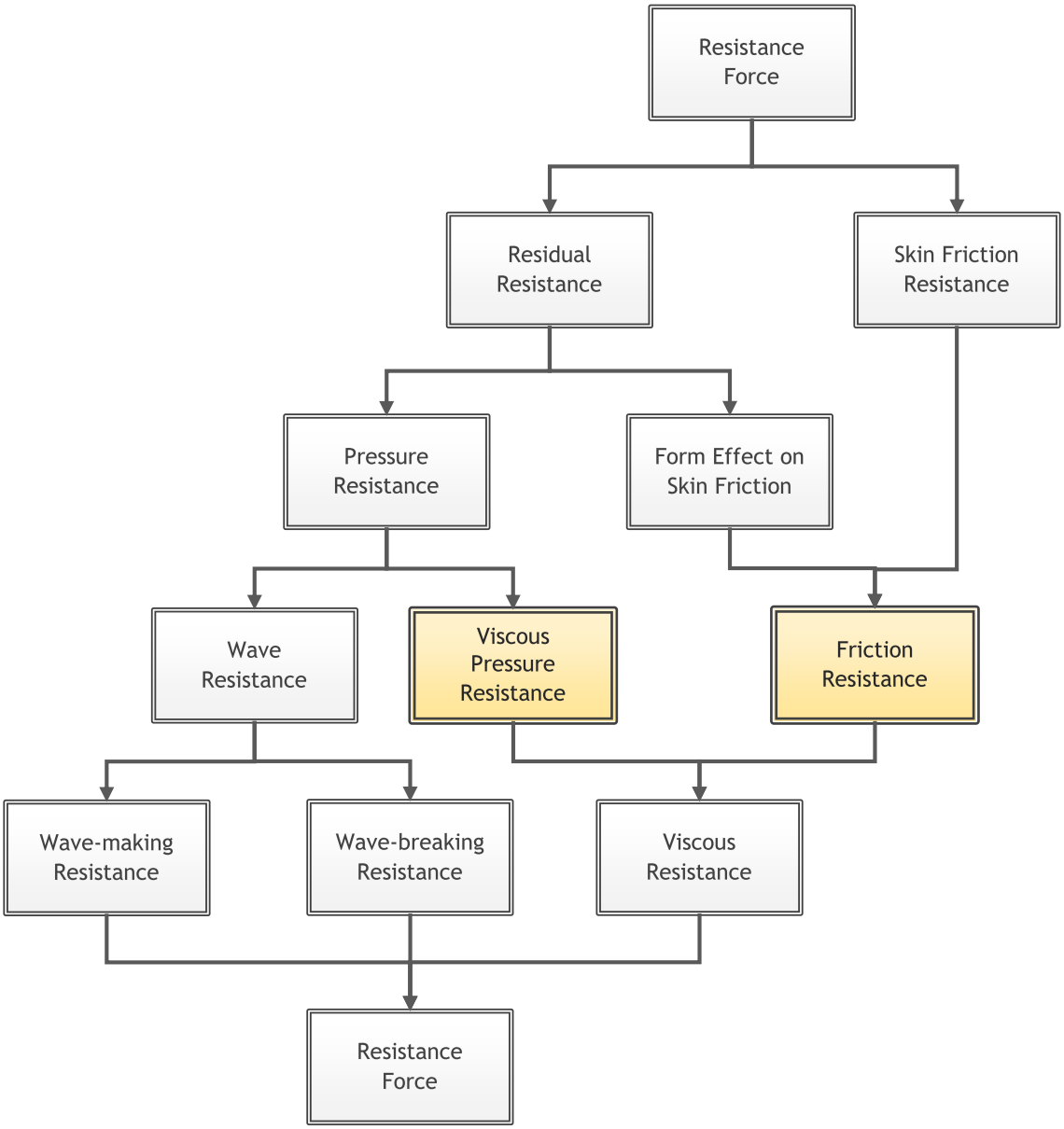

Figure 2.6 – Resistance Force decomposition (adapted from [24]).

This resistance force is represented by the relationship presented in Equation (2.1)

$$F_R = \frac{1}{2}.\rho\,.C_D\,.U^2\,.S \tag{2.1}$$

Where ρ is density, C_D the Drag coefficient, U is the model velocity and S the wetted surface area.

Following the equation above, the Drag coefficient is given by the Equation (2.2),

$$C_D = \frac{F_R}{\rho.\frac{1}{2}.U^2.S} \tag{2.2}$$

Where all parameters are known from the Equation (2.1). The author considered relevant to describe these two similar equations, since these are fundamental for this study.

Generally, the resistance force can be divided into three different components: form drag or pressure drag (also known as viscous pressure resistance), friction resistance and wave resistance. Since this study is for a fully submerged mode i.e. there is no free surface effect. Knowing that the main difference between submerged mode and surfaced mode is wave-breaking and wave-making, the wave resistance is neglected in the scope of this study. To understand the influence of free surface effect (two-phase flow condition) see E. Dawson [25]. Henceforth, a fully submerged condition is always assumed by the author. Therefore, there are two dominant factors responsible by the submerged body's resistance to motion when moving in a homogenous viscous fluid domain: friction resistance (tangential shear forces) and viscous pressure resistance (normal pressure forces) resistance, as marked in Figure 2.6.

The friction resistance coefficient is given by the Equation (2.3):

$$C_F = \frac{0.075}{(\log_{10} Re - 2)^2} \tag{2.3}$$

Where C_F is the non-dimensional frictional resistance coefficient and Re is the Reynolds number. Knowing C_F and C_D (given in Equation (2.2)) the Residual Drag coefficient (C_R) can be obtained from the Equation (2.4):

$$C_R = C_D - C_F \tag{2.4}$$

The residual drag is a significant parameter for hydrodynamic studies defined as total resistance except for skin friction drag.

The influence of each component on resistance force is dependent on the size and shape of the body, as shown in Figure 2.7. There is no precise minimum in total drag but various authors refer an optimum L/D ratio for a streamlined body is between 6 and 7. This optimum value changes depending on its shape. In order to reduce the form resistance, the hull length can be extended. However, the resultant increase in length and wetted surface area leads to an increase in friction resistance. Then, the effects of L/D ratio on the two components are contradictory, where the lowest point of total resistance force is related to the optimum L/D ratio, as shown in Figure 2.7.

Reynolds number (Re), mentioned in Equation (2.3), is an essential parameter used on this thesis for dynamic similarity between the full-scale AUV prototype and hull model used for this study. To assume similar flow conditions, applied on this case, the Reynolds number needs to be the same for both scales i.e. Reynold's law must be ensured (the inertial and frictional forces are present). For a constant kinematic viscosity (ν), the smaller the models mean the higher speed, and forces do not scale down for constant viscosity. However, this similarity is

only valid when fluid properties of both scales are the same. Due to Reynolds number appears in RANS equations, it has an effect on all flows governed by these equations. Reynolds Number (hereinafter, Reynolds Number is going to referred as Re) is defined by the ratio of the fluid's inertia forces to the viscous forces in the boundary layer of the fluid and it is given by the Equation (2.5),

$$Re = \frac{U.l}{\frac{\mu}{\rho}} \tag{2.5}$$

Where μ is absolute viscosity and l the characteristic linear dimension. The denominator is also known as (Equation (2.6)),

$$\nu = \frac{\mu}{\rho} \tag{2.6}$$

Consecutively, the Reynold's similarity is represented by the Equations (2.7) and (2.8),

$$(Re)_M = (Re)_P \tag{2.7}$$

$$U_M = U_P.(\frac{L_P}{L_M}) \tag{2.8}$$

Where the subscript M represents Model and P the full-scale Prototype.

Since Re appears in several applications, l represents one of many length scales. The transition point (point which the boundary layer changes from laminar to turbulent) is dependent of Re i.e. as Re increases, this point moves forward on the surface [26]–[29].

Another parameter which influences resistance of the streamlined body is the prismatic coefficient (C_p), that describes the amount of volume on the ends of the body. It is formed as "the ratio of the displaced volume with that contained in a prism formed by the mid-ship cross-sectional area and the length"[30]. An optimum C_p value is around 0.6 [25], [31]. The C_p is defined as (Equation (2.9)):

$$C_p = \frac{\nabla}{\frac{\pi}{4}.\ D^2\ .L} \tag{2.9}$$

Where ∇ is the volume of the envelope, D the maximum hull diameter and L the body's length. According to Joubert [30], reducing both L/D ratio and C_p "should give a reduction in total resistance coefficient of over eight percent.".

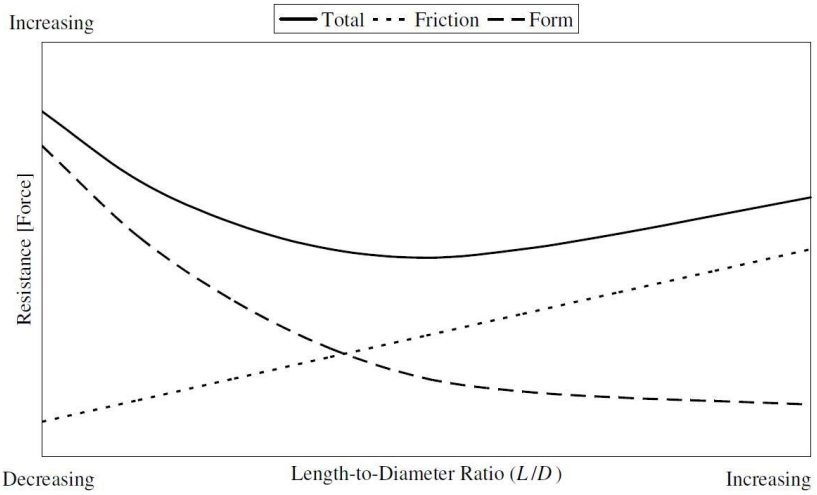

Figure 2.7 – Resistance force components for a streamlined body with constant volume in an infinite fluid domain at constant velocity (adapted from [25]).

The viscous pressure drag varies along the body's surface, being its biggest value at the nose (called stagnation point), where the streamlines divide through the body. The pressure is smaller when the streamlines are straight, and rises when are diverging. In an ideal fluid (fluid with no viscosity), the nose and tail pressure would be the same i.e. the integral of all pressures acting on the body's surface would be zero [25], [31].

However, in a real fluid, the viscosity is an important property that causes tangential force or friction resistance. This phenomenon occurs due to the interaction between the fluid and the body, and the formation of a fluid boundary layer around the body's surface. The boundary layer depends on the relative velocity, location along the body's length and the effects of local pressure gradients. The flow along the boundary layer can be either laminar or turbulent with a transitional region dividing the two [25], [31]. A detailed description of boundary layer is presented by [32], [33].

2.4.2 Hull Shape

According to the given backgrounds above, it is extremely important to choose the most efficient hull shape in order to get the lowest drag possible.

Mainly, two types of axisymmetric bodies were considered, these seem to be admitted by all authors with similar studies [8], [24], [34], [35]. These bodies are shown in Figure 2.8. A round hull presents no stress concentrations and when compared to other shapes is able to withstand more pressure, except for the spherical form. The spherical form is not considered on this study, even though being the most effective hydrodynamic shape. There are some aspects as strength, maneuverability, form resistance (L/D ratio = 1), propulsive efficiency or power housing requirements that makes this form an unfeasible option [36].

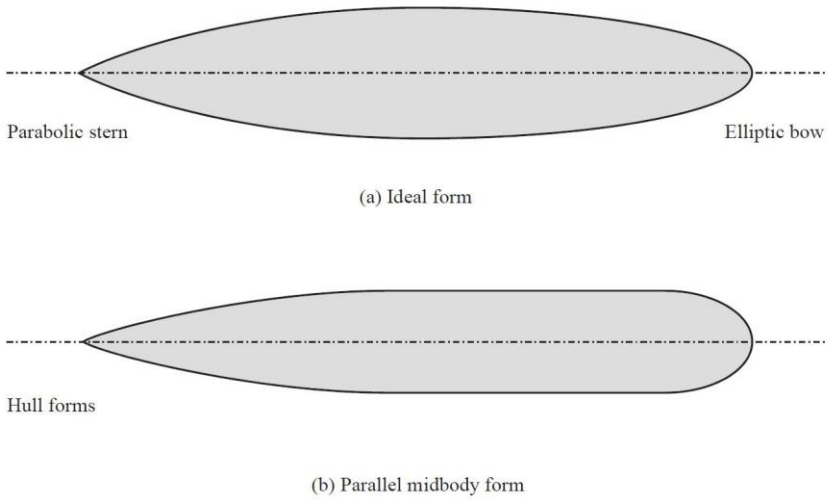

Figure 2.8 - Axisymmetric hull shapes (adapted from [31]).

On Figure 2.8 (a) the shape presented is, known as the teardrop shape, this is the most ideal shape for submerged mode. Although, due to several issues on its construction and power housing requirements, the most conventional and applied form on AUV's is the parallel mid-body form (Figure 2.8 (b)). The nose and tail form, can be elliptical, conical or even parabolic.

2.4.3 Restrictions to the flow around the model

Depending on the model's and tank size, there are some differences when an AUV model is towed in a towing tank or in the unrestricted water. These differences are usually referred to as the boundary effects. It may be classified into Wall Effect, Free surface effect and Blockage Effect [37].

The blockage ratio is defined as "the ratio of the maximum cross sectional area of the model to that of the towing tank." [37]. Following this definition, the Blockage ratio is given by the Equation (2.10),

$$Bl = \frac{a}{S_O} \tag{2.10}$$

Where a is the maximum cross sectional area of the model and S_O the maximum cross sectional area of the towing tank.

Wall Effect only depends on tank's width. A combination of limited width and depth is known as the Blockage Effect. This phenomenon is rather complex due to the interference of the tank sides and bottom i.e. model size has to be sufficiently small to avoid inherent hydrodynamic interference, and this is called reflected wave interference effects. Unfortunately, a model too small leads to additional inaccuracies on the quality of results obtained due to the similarity between the full scale prototype and the model test [37]. As a result, the largest model with

minimum interference induced must be found. During the last years, the International Towing Tank Conference (ITTC) [38] made a recommendation for finding a blockage correction, although there is a lack of literature available. The blockage ratio is the most important parameter of the blockage effect. Marine Renewables Infrastructure Networks (MARINET) [39] refer blockage ratio above 0.1 can introduce questionable results, whereas H.Kim and J.Moss [37] present a lower limit of blockage ratio below which the blockage effect has normally been considered to be insignificant is 0.006. However, MARINET also refer cases which wave making is small, could be used larger models with the appropriate correction for the remaining blockage effect [37], [39], [40].

As described previously, AUV's have two modes of navigation: surfaced mode and submerged mode. In surface mode, the wave resistance (divided into two components: wave breaking and wave making) is a main part of resistance (up to 50%) of total resistance. Although, this thesis is only based on the submerged mode, however, to travel under water, it is important to know at which depth is the interference of free surface negligible i.e. the wave resistance is minimum and can be neglected [24], [35]. There are several studies to find this fully submerged condition.

Hoerner and Weinblum et al. [25] concluded that for submergence depth-to-diameter ratios of at least 5 (H* = 5.00) the wave resistance could be neglected, where H* is defined as (Equation (2.11),

$$H^* = \frac{h}{D} \tag{2.11}$$

Being h the submergence depth of an axisymmetric body's longitudinal centerline below the still waterline and D the maximum diameter.

There are other authors that connected the fully submerged depth with maximum diameter or length of submersible hull. According to Moonesun et al. [24] several authors used different submerged depths for their studies as, $h = L/2$, $h = 3D$ or $h = 5D$. Figure 2.9 shows the effect of the submergence depth on Drag Coefficient.

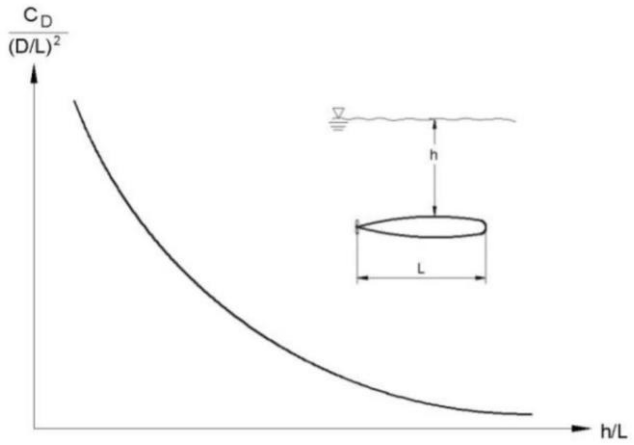

Figure 2.9 - Total resistance coefficient vs Submergence depth (adapted from [24]).

Moreover, Moonesun et al. [24] compares this submergence depth with Froude number (Fn) and concludes that it is an important parameter in the evaluation of submergence depth. Also concludes that exists one "Milestone depth" where wave resistance decreases more than 80% and other where there is no wave resistance called "Fully submerged depth", as shown by the references above and as can be seen in Figure 2.10. Further, this author refers the "fully submerged depth for high Froude numbers is equal to 4.5D." and the "milestone depth for high Froude numbers is equal to 0.125L.". Moonesun et al. [24] presented the Froude number as a crucial parameter to study submergence depth, showing that for Fn < 0.5 were considered ordinary values and for Fn > 0.7 high values. These statements are supported by Figure 2.10.

The Froude number appears in two-phase flow conditions (problems involving pressure boundary conditions) and it is only important for determining which depth there is no wave resistance. Since this thesis focus on one-phase flow condition, Froude number is only helpful to comprehend which depth is the fully submerged condition i.e. this means that if there is no free surface, this parameter is insignificant, as well as Weber and cavitation number (insignificant numbers for this thesis) [26], [28]. Fn is given by the Equation (2.12).

$$Fn = \frac{U}{\sqrt{gL}} \tag{2.12}$$

Where g is the acceleration due to gravity, and L is the waterline length of the vessel.

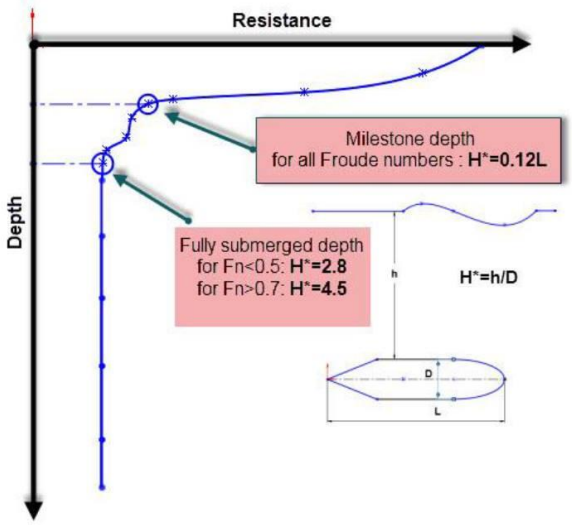

Figure 2.10 - According Moonesun et al., Milestone and fully submergence depth for all Froude numbers (adapted from [24]).

2.5 Fluid Mechanics Foundations

Before examining the methods of Computational Fluid Dynamics, a review of the governing equations of fluid mechanics must be done.

The fluid is defined by the ratio of specific heats (γ), viscosity (μ) and the coefficient of heat conduction (κ). The motion of the fluid is controlled by governing equations and boundary conditions. Based on conservation laws, the governing equations of fluid mechanics are given by:

- Mass conservation equation or continuity equation (mass can be neither created nor destroyed);
- Momentum conservation equation (Newton's 2nd Law);
- Energy conservation equation (based on the 1st law of Thermodynamics).

All details of these equations (considerations and forms) are fully described at references [41], [42]. Hence, only the final equations will be demonstrated.

The conservation of mass can be described as the net outflow of mass through the surface surrounding the volume has to equal to the time rate of decrease of mass inside control volume. The differential form of continuity equation (vector form) is given by the Equation (2.13):

$$\frac{D\rho}{dt} + \rho\,.(\nabla\,.q\,) = 0 \tag{2.13}$$

Where t is the time, q is fluid velocity vector (μ, v, w) and $\frac{D}{d_t} = \frac{\delta}{\delta t} + q\,.\nabla$ is the material derivative that represents the rate of change following a fluid particle [43], [44].

The momentum conservation equation, based on Newton's 2nd law of motion, is represented by the Equation (2.14), which represents the net force action on a system has to be equal to the time rate of change of momentum of system.

$$\rho \frac{Dq_i}{Dt} = \rho f_i + \frac{\delta \tau_{ij}}{\delta x_j} \tag{2.14}$$

Where f_i is the component of the mass force per unit mass second in the i direction, τ_{ij} are the stress components, and $i,j = (1,2,3)$, i.e. a matrix 3x3 of stress components. Assuming a Newtonian fluid (where the stress components are linear to the derivatives), a relation between velocity filed and stress components can be made, as shown in Equation (2.15) [44].

$$\tau_{ij} = \left(-p - \frac{2}{3}\mu \frac{\delta q_k}{\delta x_k}\right)\delta_{ij} + \mu\left(\frac{\delta q_i}{\delta x_j} + \frac{\delta q_j}{\delta x_i}\right) \tag{2.15}$$

Where μ is the viscosity coefficient, δ_{ij} is the Kronecker delta function, p is the pressure and k a dummy variable summed from 1 to 3. Replacing the stress components of Equation (2.15) into the Equation (2.14), the Navier-Stokes equations are achieved, as demonstrated in Equation (2.16).

$$\rho\left(\frac{\delta q_i}{\delta t} + q\,.\nabla q_i\right) = \rho f_i - \frac{\delta}{\delta x_i}\left(p + \frac{2}{3}\mu \nabla\,.\,q\right) + \frac{\delta}{\delta x_j}\mu\left(\frac{\delta q_i}{\delta x_j} + \frac{\delta q_j}{\delta x_i}\right) \tag{2.16}$$

Finally, to complete the system of equations comes the energy conservation equation, which states the 1st Law of Thermodynamics: "The sum of the work and heat added to a system will equal the increase of energy."[45]. There are several forms of this equation in literature, the Equation (2.17) is one of these forms.

$$\frac{D\rho(e + \frac{1}{2}V^2)}{Dt} = \nabla.(K\nabla T) - div\mathrm{w} \tag{2.17}$$

Where K is the coefficient of thermal conductivity, e is the internal energy per unit mass, T is the temperature gradient, w is the vector of work associated with each control volume face and $-div\mathrm{w} = \dot{W}$ the work done on the system [46].

2.6 Computational Fluid Dynamics (CFD) – Numerical Approach

The behavior of viscous fluid flow is described by Navier-Stokes Equations (Equation (2.16)). Fluid flow, in of the majority of the cases, is turbulent. Turbulent flows have as particular characteristic: transportation of quantities, as momentum, energy, and species concentration, with fluctuation (hardest case to solve, small scale and high frequency) [47], [48]. These complex equations need to be solved numerically by the use of computational methods, except for very simple cases. All of these computational, theoretical and numerical methods are known as Computational Fluid Dynamics.

The computational fluid mechanics techniques use the Eulerian approach to solve all applications. However, Navier-Stokes equations varies with time, which denotes that is required averaging multiple solutions at a set of time steps [49]. This leads to a decomposition of Navier-Stokes equation into the Reynolds Averaged Navier-Stokes (RANS) equations. Furthermore, RANS equations introduces to a several unknowns (Reynolds stress) that requires a turbulence model to generate a closed system of solvable equations, i.e. turbulence model is used to close the system of mean flow equations [49].

RANS equations are the most widely used approach, although there are other approaches that can simulate with higher precision, as Large Eddy Simulation (LES) or Direct Numerical Simulation (DNS). LES solves the spatially averaged RANS equations, directly resolving larger eddies, but modelling small ones. However, due to the computational requirements it is not a feasible option. DNS solves the full RANS equations, simulating with accuracy all turbulent flows (all eddies included) without requiring turbulence models. However, this approach is not practical for engineering purposes, due to extremely high costs and computational resources required [50]. A more detailed study about this topic can be made by checking of references [29], [31], [42], [51] .

2.7 Turbulence models

Since this study comprises the use of a well-known commercial software called ANSYS FLUENT, it will be described the turbulence models related to this tool.

Therefore, the turbulent models provided by ANSYS FLUENT are:

- Spalart-Allmaras model (one-equation model);
- κ-ε models (two-equation model)
- Standard κ-ε model;
  - Renormalization-group (RNG) κ-ε model;
  - Realizable κ-ε model.
- κ-ω models (two-equation model)
  - Standard κ-ω model;
  - Shear-stress transport (SST) κ-ω model.
- Reynolds Stress Model (RSM) (seven-equation model);
- Large Eddy Simulation (LES) model.

It is important to understand “that no single turbulence model is universally accepted as being superior for all classes of problems” [50]. So, depending on purpose/necessity and computational resources/time efficiency the choice of turbulence model should be made. Following this procedure and the ideas reached by literature review, two models will be described. These turbulence models are: Standard κ-ε and κ-ω SST models. A detailed information about these models or other turbulence models are fully presented in [42], [50].

2.7.1 Standard κ-ε model

This is the most used turbulence model in engineering for industrial applications. It is known as being robust, economic and with a satisfactory accuracy for turbulent flows. As referred above this is a two-equation model, which allows to calculate the turbulent length and time scale by solving two transport equations. These equations are for turbulence kinetic energy (κ) and dissipation rate (ε). A limitation of this turbulent model is that it is only valid for fully turbulent flows. Further, at near-wall regions, wall functions must be used, due to ε equation. Although, several improvements were implemented on Standard κ-ε model, resulting in examples as κ-ε RNG model or κ-ε Realizable model, but as referred previously, a trade-off of purpose/computational resources should be made before choosing a turbulent model [48].

2.7.2 κ-ω SST model

This turbulence model is considered an "upgrade" of Standard κ-ω. Furthermore, it was developed to have the benefits of κ-ω model (near-wall region) and κ-ε model (freestream independence in the far field). The ω equation integrates a damped cross-diffusion derivative term. The consideration of the transport effects of the principal turbulent shear stress led to a modified turbulent viscosity formulation [42], [50].

2.8 Similar studies

Mansoorzadeh and Javanmard [52] presented the free surface effect on drag and lift coefficients of an AUV by comparing two-phase flow numerical simulation with single phase flow simulation and the experimental procedure. The study was performed at several submergence depths for 1.5 and 2.5 m/s. The study demonstrated that, for both AUV speeds, the influence of free surface on drag coefficient was decreasing as the model distance from the free surface was increasing. A maximum difference of 10% between the numerical and experimental results for drag coefficient was observed. These authors concluded that it is not very straightforward to compare which method is more accurate, since there are errors and uncertainties associated with each one. Although, collecting data from both methods and compare them seemed to conclude better results.

J.L.D. Dantas and E.A. de Barros [11] investigated the hydrodynamic forces and coefficients obtained by an AUV with control surface deflection and angle of attack by the use of CFD software based on the Reynolds-Averaged Navier-Stokes (RANS) equations. These authors conducted their CFD simulations separately (AUV bare hull and control surface), to better predict each interference and compare with experimental results obtained in a towing tank. They concluded that the k-ω SST turbulent model was the best model to predict hydrodynamic coefficients and the nonlinear regression methodology is the best choice for predicting the stall at control surface.

For these experimental results done by J.L.D Dantas and E.A. de Barros [11], Lucas et al. [53] used strain gauge type dynamometers to measure hydrodynamic efforts of an AUV with the same external geometry used by Maya AUV, with a diameter of 0.234 m and a total length of 1.742 m, at a longitudinal velocity of 1 m/s. In order to measure hydrodynamic forces and moments, experiments were made for each sideslip angle, adopting some struts configurations to reduce its influence in results (Drag and hydrodynamic effects). Experiments indicated, in the normal force case, an insignificant difference using the fairing structure. The results are shown in Figure 2.11 with a comparison of the results obtained by other author (Jorgensen) with similar study [8]. Furthermore, De Barros, Dantas, Pascoal and De Sá [54] used some of these results to create a new application methodology of semi-empirical prediction models.

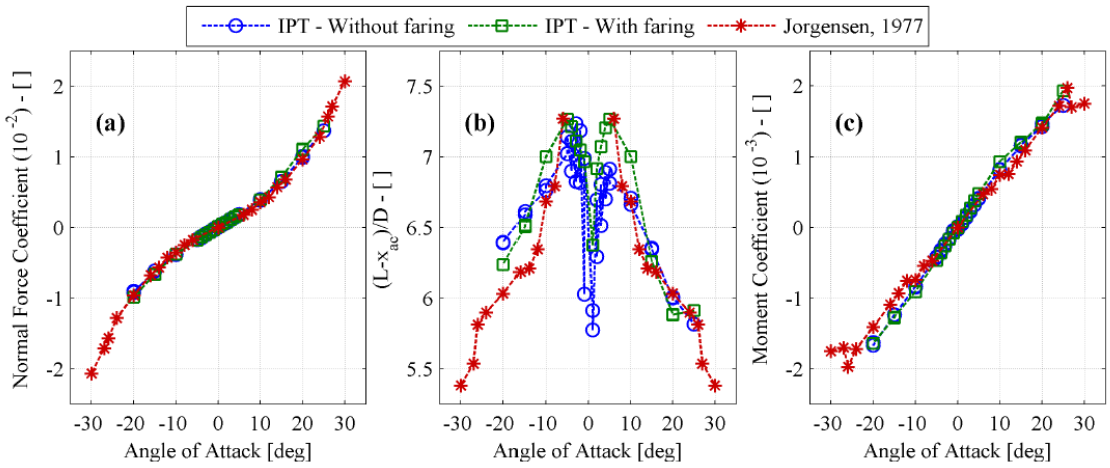

Figure 2.11 – Comparison of normal force coefficient (a); hydrodynamic center (b) and pitch moment (c) between towing tank results and Jorgensen results (adapted from [8]).

Praveen P.C. and Krishnankutty P. [34] studied the hydrodynamic forces of axisymmetric UUV's by varying vehicle's length due to angle of attack, for a bare hull configuration, by performing Vertical Planar Motion Mechanism (VPMM) experimental tests, using CFD code FLUENT 6.2. for numerical simulations and doing the same Analytical and Semi-Empirical (ASE) method that De Barros, Dantas, Pascoal and De Sá used [54]. Their numerical and experimental results were converging and the empirical method seemed to be very good to predict linear coefficients. Results show that the linear coefficients vary linearly with L/D.

P.Jagadeesh and K.Murali [55] studied four low Reynolds number k-ε models to predicting the hydrodynamic forces of AUV's. These authors demonstrated that the k-ε Abe-Nagano-Kondoh (AKN) turbulent model revealed to predict more closely the flow separation and wake formation in comparison to the other models considered. This turbulent model has also shown a better hydrodynamic coefficients prediction when compared with other models.

P.Jagadeesh, K.Murali and V.G.Idichandy [56] performed an experimental study on hydrodynamic forces and moments of an AUV model in the vertical plane to observe its variation with Reynolds number and angle of attack. To validate these results, CFD ANSYS FLUENT with RANS equations was used. Using the Froude scaling, a model scale ratio was selected. The turbulence model k-ε AKN showed to be a good option for predicting hydrodynamic forces and coefficients of AUV's. It was also shown that there was a maximum increase in normal force coefficient compared to axial force coefficient under the same conditions (velocity and angle of attack). Equally, for the pitching moment, lift and drag coefficients there is an increase of these values.

Alam, Ray and Anavatti [57] presented empirical and numerical (CFD ANSYS FLUENT 13.0.) methods to estimate the drag of an AUV. The range of flow speed varied from 0.5 to 3.0 m/s, with a range of Reynolds number of 6.5×10^5 to 3.89×10^6. The turbulent model used by authors was the realizable k-ε model with enhanced wall treatment. Results show good agreement with empirical estimation, although drag differences between the empirical and CFD results increase at high velocities (10.80% at a flow speed of 3.0 m/s).

Moonesun, Javadi, Charmdooz and Mikahailovich [35] presented a detailed experimental procedure to test a model scale ratio of 1:32 of the prototype vehicle. Since the scale was too high, Reynolds number similarity was unfeasible. Therefore, the authors adopted four other methods for scaling, found depth which there is no free surface effects (five times the model's diameter) and a CFD simulation was made to compare. To predict which was the best method, authors made a comparison between model tests and the other five tests (four empirical estimations and one numerical simulation). CFD simulation showed the best results for hull and appendages analyses (10% of error at a speed of 12 knots).

Kunz et al. [58] conducted an expedition called the Artic GAkkel Vents Expedition (AGAVE) to further investigate marine biology, chemistry and geology associated with hydrothermal venting at Gakkel Ridge. Two AUV's (Jaguar and Puma), differing only in their sensor payload, were designed to perform the task of collecting images and samples of the deep seafloor. These AUV's are based on Seabed design and performed a total of nine dives at depths of up to 4062 m. Authors concluded that "the fundamental requirement for reliable acoustic communications should be taken as a starting point for future development of sub-ice vehicles.".

In fact, this is not directly connected to the topic of this thesis. However, the AUV's (Jaguar and Puma) geometries are similar to the prototype that this thesis is based on. Consequently, it is pertinent to highlight a similar project and its mission; it can be seen as a guide.

Chapter 3

3 Case Study

It is aimed to optimize the hydrodynamics of a single-hull body considered as representative of MEDUSA Deep-Sea lower-hull, in order to optimize the external vehicle shape for the operation conditions. Furthermore, an optimized external vehicle shape produces lower Drag force, which reduces the energy consumption of the vehicle, and consequently increases its autonomy. As well as MEDUSA Deep-Sea, the single-hull prototype is considered to operate in depths up to 3000 m in ocean (salt water), i.e. resist to a pressure of at least 300 atm. Vehicle should also hold Temperatures up to a minimum of 0˚C.

3.1 Requirements

The prototype is also considered to operate in velocities between 0 and 3 m/s, with a nominal operation velocity of 1.5 m/s. Moreover, operating at its nominal operation velocity, the vehicle should not sustain operations at AoA's higher than 20˚, being its nominal cruise operation at 0˚. These operation conditions are represented in Table 3.1.

Table 3.1 - Prototype's Operation Envelope.

Velocity [m/s]	0.15 – 0.30 – 0.45 – 0.60 – 0.75 – 0.90 – 1.05 – 1.20 – 1.35 – 1.50 -1.65 - 1.80 – 1.95 – 2.10 – 2.25 – 2.40 – 2.55 – 2.70 – 2.85 – 3.00
Angle of attack [degrees]	0 – 5 – 10 – 15 - 20

3.2 Dimensions and Shape

Throughout systems, structural and stability constraints, the dimensions of the single hull body considered as representative of prototype's hull were defined. These considered dimensions were: centre section diameter of 0.340 m and a length of 1.5 m.

According to the literature review and respecting the given design constraints, the most appropriate shape for the centre section is the cylindrical shape. In order to improve the hydrodynamics, nose and tail hydrodynamic fairings were included. These nose and tail sections were studied to understand which shape specifically should be used. This study includes the elliptical and conical shapes for the nose and tail fairings. However, the properly nose and tail length must be also found to fully optimize the hull prototype. Classification of the tail and

nose shapes is done using an appropriate characteristic dimension ratio. N/D is the ratio of the nose length over the hull's diameter and T/D is the ratio of the tail length over the hull's diameter. The Figure 3.1 shows all the hull's configurations studied.

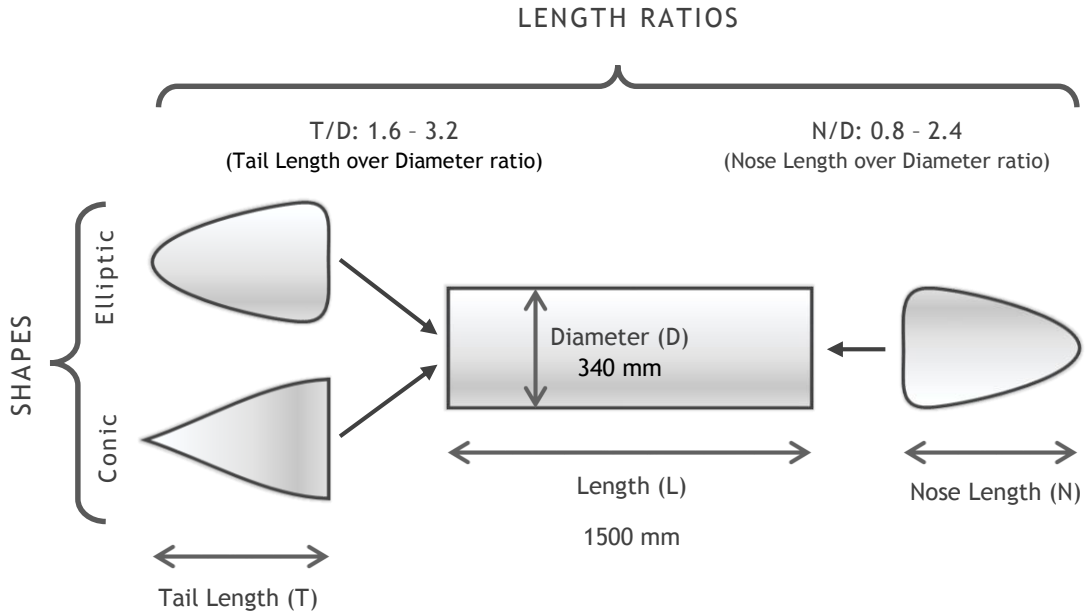

Figure 3.1 - Characteristics (dimensions, ratios and shapes) of all components of full-scale prototype used for this study.

Chapter 4

4 Experimental Study

In this Chapter, the experimental procedure will be fully detailed, including the several considerations and steps made. Further, the results of the experimental tests will be shown, demonstrating the tendencies obtained from the data collection.

4.1 Experimental Model Design

4.1.1 Dimensions

Due to towing tank size (see Table 4.1), a full-scale single-hull model was an unfeasible option. Therefore, the first consideration taken to Model's Design was to find an optimum trade-off between model's and tank size, i.e. higher Model length can induce to Wall and Surface effects, and smaller Model length can induce to scale error effects (associated with scale ratio). Thus, a L_{TOTAL}/D ratio = 10 was defined as starting Design point. According to the authors referred above, finding the largest model without wall and free surface interference must be a focus. Following these authors and knowing the size of the tank (Table 4.1), the depth for fully submerged condition has been calculated, as shown on the Tables (Table 4.2 & Table 4.3) below. The difference between the Tables is only considering the diameter while measuring the h, i.e. considering h from the hull's surface or body's longitudinal centerline.

Table 4.1 – Towing tank dimensions.

Towing Tank	
Height [mm]	800
Width [mm]	800
Length [mm]	12000

Table 4.2 - Model's parameters according full scale prototype (h considered since the body's longitudinal centerline to water's surface).

	Full -Scale Prototype	Depth --> h = 400 - D/2 [mm]				
		L/2	3D	5D	4D	6D
$Length_{Total}$ [mm]	2400.0	727.3	1142.9	727.3	888.9	615.4
Diameter [mm]	240.0	72.7	114.3	72.7	88.9	61.5
L/D ratio	10.0	10.0	10.0	10.0	10.0	10.0
L_{body} [mm]	1160.0	351.6	552.4	351.5	429.6	297.4
L_{nose} [mm]	530.0	160.6	252.4	160.6	196.3	135.9
L_{tail} [mm]	710.0	215.2	338.1	215.2	263.0	182.1
L_{Nose}/D	2.2	2.2	2.2	2.2	2.2	2.2
L_{Tail}/D	3.0	3.0	3.0	3.0	3.0	3.0
Velocity - V[m/s]	0.3	0.8	0.5	0.8	0.7	1.0
	0.5	1.7	1.1	1.7	1.4	2.0
	0.8	2.5	1.6	2.5	2.0	3.0
	1.0	3.3	2.1	3.3	2.7	3.9
	1.3	4.1	2.6	4.1	3.4	4.9
	1.5	5.0	3.2	5.0	4.1	5.9
H*		5.0	3.0	5.0	4.0	6.0

Table 4.3 - Model's parameters according full scale prototype (h considered since the body's surface to water's surface).

	MEDUSA_DP (Lower Hull)	Depth --> h = 400 [mm]				
		L/2	3D	5D	4D	6D
$Length_{Total}$ [mm]	2400.0	800.0	1333.3	800.0	1000.0	666.7
Diameter [mm]	240.0	80.0	133.3	80.0	100.0	66.7
L/D ratio	10.0	10.0	10.0	10.0	10.0	10.0
L_{body} [mm]	1160.0	386.7	644.4	386.7	483.3	322.2
L_{nose} [mm]	530.0	176.7	294.4	176.7	220.8	147.2
L_{tail} [mm]	710.0	236.7	394.4	236.7	295.8	197.2
L_{Nose}/D	2.3	2.2	2.2	2.2	2.2	2.2
L_{Tail}/D	3.0	3.0	3.0	3.0	3.0	3.0
Velocity - V[m/s]	0.3	0.8	0.5	0.8	0.6	0.9
	0.5	1.5	0.9	1.5	1.2	1.8
	0.8	2.3	1.4	2.3	1.8	2.7
	1.0	3.0	1.8	3.0	2.4	3.6
	1.3	3.8	2.3	3.8	3.0	4.5
	1.5	4.5	2.7	4.5	3.6	5.4
H*		5.0	3.0	5.0	4.0	6.0

As shown above, the main difference between TablesTable 4.2 andTable 4.3 lies in the depth h (400 or 400-D/2). The author selected these dimensions, due to towing tank size (height and width middle point). At this point, h, the influence of both side walls is the same and the author assumed the same influence on tank's surface and bottom. In fact, the influence of water's surface and bottom tank wall is not the same, but according to literature review (Froude number, submergence depth and blockage ratio) and to the towing tank restrictions seemed to be the most feasible option. Thus, according to the literature review [24], at least H* = 3 must be respected for a fully submerged depth. The author preferred to follow the second Table (Table 4.2), in order to get the largest model. The columns marked as light grey, were the conditions chosen to follow. In this case, it is relevant to understand that the h = L/2 and h = 5D have the same results. The only difference between each condition is the point where the calculation starts i.e. for L/2 the first step is to find the total length and for 5D is to find the maximum diameter. Therefore, the largest model and a fully submerged depth were found to be respecting all the conditions referred above. A smaller model could be used to do the experiments, like for example the h = 6D calculated by the author. However, the smaller the model, the bigger the errors associated with scaling process. Thus, to guarantee Reynold's similarity, a smaller model needs to achieve a bigger velocity as shown by Equation (2.5).

As it will be shown in the Experimental Setup, the tank's depth is not always constant. However, several procedures were made to guarantee the data collection at the location which has the desired tank depth (800 mm).

Applying the Equation (2.10) on this study, the blockage ratio is given by the Equation (4.1),

$$\frac{(80\,.\,80)}{(800\,.\,800)} = 0.01 = Bl \tag{4.1}$$

The author uses a blockage ratio of 0.01, for low Froude numbers (always smaller than 0.7) and small wave making as will be shown later. Therefore, the blockage effect has no influence on results or it is too small that will be ignored [39].

In order to optimize the AUV model, various experimental conditions were defined, after the restrictions found due to the towing tank size, with different nose and tail ratios to find the optimum configuration. Based upon the premise of Figure 3.1 and Table 4.2, all Lengths (Nose, mid-body and Tail) were calculated. Thus, ratios were discussed and defined to have a logical manner of evaluate the body's model, keeping constant the mid-body's diameter and length, varying only the Nose and Tail lengths. Adapting the full-scale case from Figure 3.1 to the AUV model, due to all restrictions, the hull's dimensions and ratios were calculated, as can be shown in Figure 4.1.

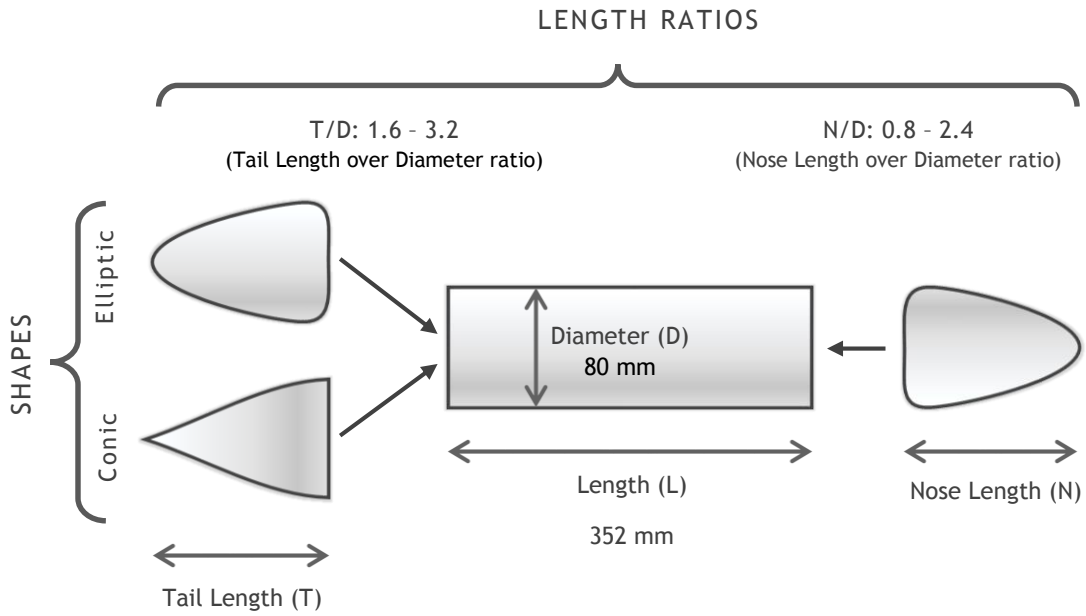

Figure 4.1 - Characteristics (dimensions, ratios and shapes) of all components of AUV model used for this study.

4.1.2 Prototype Design & Manufacturing

In this section is demonstrated the process of model's design and crucial considerations adopted until its manufacturing. Besides the design of the AUV model, helpful tools were also designed to adapt and get easier to the experiments. Thus, this section can be known as the starting point for the Experimental Setup that will be described later on this Chapter.

The software used to design this experimental procedure was the CATIA V5R24 powered by Dassault Systèmes [59]. CEiiA provided the use of this commercial software.

It is important to denote that due to several manufacturing limitations, some geometrical precautions were taken such as curvature coefficient of nose and tail, and the production of a perfect conical edge was extremely difficulty to manufacture, leading to a few design adjustments.

In order to optimize the experimental procedure, all connections were screwed to simplify the process, as can be shown in Figure 4.2. In order to connect the AUV to the trolley's towing tank a detailed study was made. The holes observed on body's top connect the body to a towing tank carriage. Figure 4.3 shows an isometric view of the experimental design.

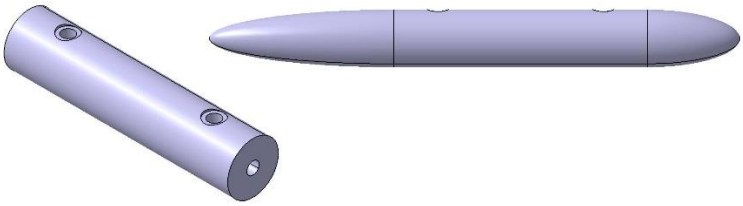

Figure 4.2 - Left image shows the body without nose and tail. Right image shows the body with an elliptical nose and tail.

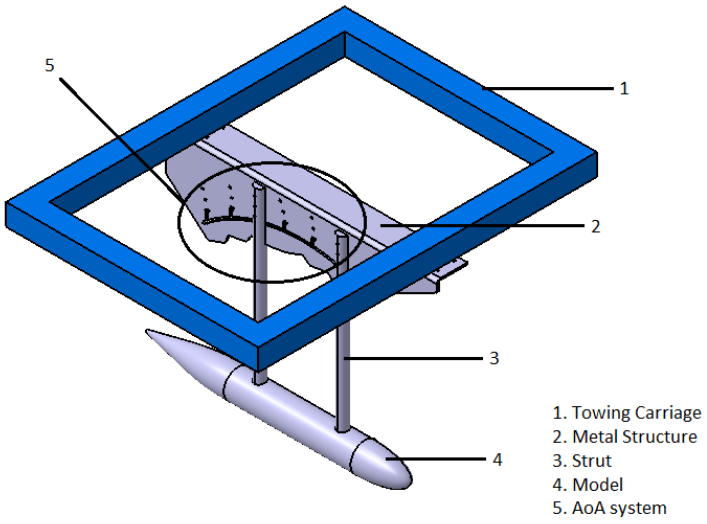

Figure 4.3 - Experimental configuration.

The AoA system (Figure 4.3 - Point 5) was designed to ensure a proposed angle of attack. In this experimental case, three AoA were desired to do the experiments, as previously shown. These three AoA are shown in Figure 4.4.

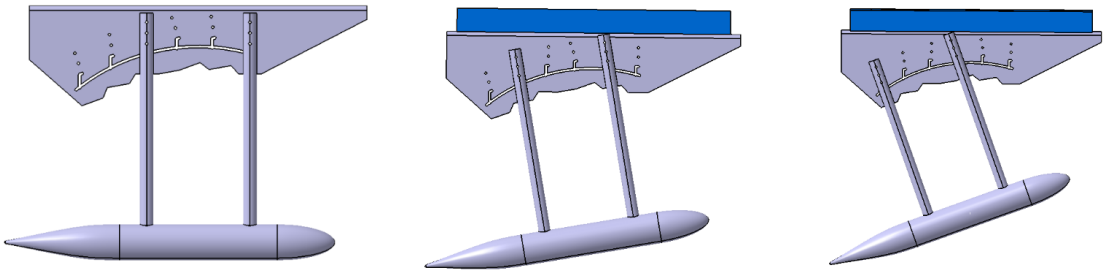

Figure 4.4 - AoA system: left) 0 degrees; middle) 10 degrees; right) 20 degrees.

Figure 4.5 shows a final arrangement of all the components manufactured with respect to Experimental procedure. However, Figure 4.5 do not include all noses and tails, only a complete experimental configuration. As can be shown, a pair of fairings were designed to reduce the resistance force generated by the struts.

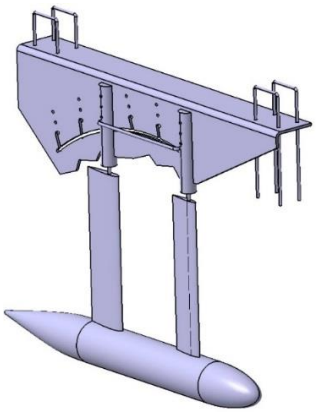

Figure 4.5 - Experimental manufactured components.

The associated Images of the final prototype after all the manufacturing processes are presented in Appendix A. Several different materials were used for this process. All components involving the AUV model (nose, body and tail) and struts were constructed using aluminum 2030 by machining process (Computer Numeric Control (CNC)). Fairings were developed by an additive manufacturing technology called Selective Laser Sintering (SLS) using Polyamide. The metallic structure that holds the struts was created by bending process using steel.

4.2 Experimental Setup

On this section, the author gives the relevant information about every milestone relative to the Experimental Setup.

The experiments were conducted in a towing tank at UBI's Hydraulic Laboratory. Knowing that running the experiments with ocean salt water was not possible, the towing tank was filled with fresh water taken from a waterhole by the use of a water pump. The water properties are shown in Table 4.4. Further, the towing tank dimensions considered are also shown in Table 4.4. The towing tank depth is not constant along the tank, being also 0.5 m depth in some sections, as shown in Figure 4.6. Nevertheless, the author considered only the section of 0.8 m depth for present studies, since the towing carriage needs a section to increase its velocity until reaching the desired velocity, and a section to decrease its velocity until it fully stops. Due to a few towing tank irregularities it was also observed that this section which the depth is 0.8 m was the most reliable zone of the towing tank for data collection. Images of the real experimental layout are shown in Appendix B.

Table 4.4 – Fluid and Towing tank properties.

Temperature	26 [°C]	**Length**	12 [m]
Density	996.787 [kg/m^3]	**Width**	0.8 [m]
Viscosity	0.00085 [kg/(s.m)]	**Depth**	0.8 [m]

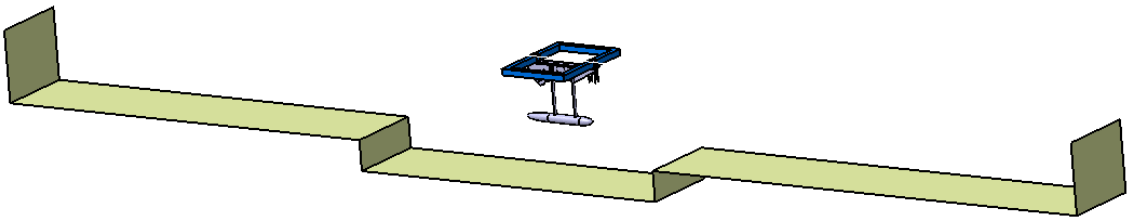

Figure 4.6 - Experimental laboratory layout.

Attending to the conditions imposed, exhibited in Table 4.5, the author encountered a major problem to solve, since the towing tank had no system to automatically tow the carriage by a given velocity. Thus, changes should be made to have a system for data collection. To settle this issue, the towing tank was adapted after several considerations. The design of full operational experimental layout is shown in Figure 4.7.

Table 4.5 - Experimental conditions; *Elliptical shape; Elliptic and Conical shapes.

U [m/s]	AoA [˚]	L_{Mid}[mm]	L_{Nose}[mm] *	L_{Tail}[mm] **	D[mm]
0.50 – 0.75 – 1.00	0 - 10 - 20	352	64 - 128 - 192	128 - 192 - 256	80

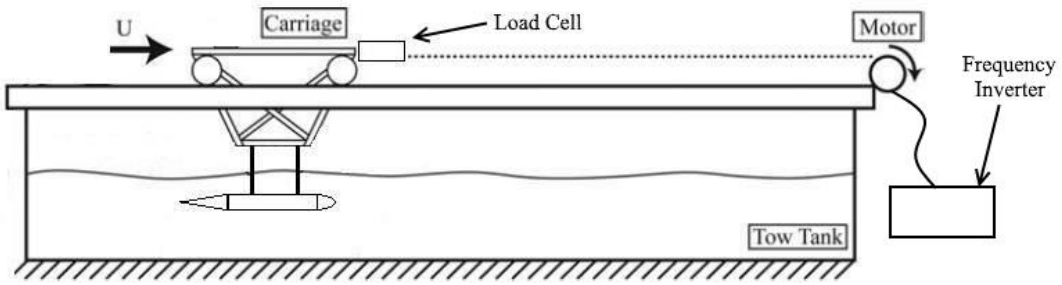

Figure 4.7 - Full experimental design.

The Load Cell (Dynamometer), showed in Figure 4.7, was used to estimate the total resistance force of the towing carriage. It was connected to the carriage and to an iron thread which was pulling the carriage driven by a motor. However, this three-phase motor used was not directly controllable, so a frequency inverter was used to control motor velocity. So, before starting any Experimental Test, a long construction process was undertaken. Some steps can be observed in Appendix C.

The materials **successfully** added to the experimental setup are listed below:

- Load cell MAX LOAD 1 ton;

- Three-phase motor 0.75 kiloWatt (kW) (1 horsepower (hp));
- OMRON V1000 50 Hertz (Hz) frequency inverter;
- Pair of polies taken from a Toyota Carina engine;
- Iron thread;
- Toothed belt;
- Aluminum (base is fully made of this material);
- Sheave;
- Solid aluminum rod;
- Iron tube (bobbin);
- Pair of bearings;
- Wood disks;
- Metallic disks;
- Circuit breaker.

To get the final and desired prototype some processes had to be used, such as:

- Metal Inert Gas (MIG) welding;
- Arc welding;
- Grinding machine;
- Mechanically powered saw;
- Turning machine;
- Laser cutting machine;
- Spray painting.

As any Experimental Procedure, this one was also made by attempts. The author made many design changes, changed several specific materials and tried to solve the problems that appeared along the way. In Appendix C a few different components from the final product can be observed (as different three-phase motor or bobbin), since in a project design there are always changes. The Figure 4.8 shows the final prototype ready to be assembled to the towing tank walls.

Figure 4.8 - Final metallic structure assembled before mounting at the towing tank.

The author also made the electric connections between the three-phase motor and the frequency inverter. The cable was inserted in the white connector, observed in Figure 4.8, and then the three-phase connection on both components were made; the three phases should work in sequence, otherwise the three-phase motor would not work. The frequency inverter is also shown in Appendix D. Figure 4.9 showing the point which the Experiments started. Further, a few adjustments in the towing tank were also executed, as the use of a caulking gun to fully close the gate and rails correction.

Figure 4.9 - Final Experimental Setup.

To optimize the Experiments (time and difficulty) an automated returning system, i.e. a system which allowed the towing carriage to go back autonomously to the starting position, was developed. A Figure of this “returning system” is shown in Appendix C. This system simplified the Experimental Procedure, since without it a run would take three times longer than it did.

There are also several considerations made by the author during the Experiments. Each of this Experiments consists of: a stationary phase (initial position); an accelerating phase until reaching the desired velocity and then remains constant for data collection; and a decelerating phase until the carriage stops in a safety mode (final position). In fact, data collection was made along the entire run and only after data analyzing the desired range was selected. Although, these Experiments depend on various factors during each data collection (instruments, stationary water, initial and final position, dynamometer precision and others), i.e. there is an uncertainty value associated in the resistance force during each data collection. Therefore, the ITTC [60] described the importance of repeat measurements at least 10 times for each specific combinations as a better measure of uncertainty. Based on this, the author defined that 10 samples should be measured for each combination.

4.2.1 Data Collection

A load cell was used to measure the resistance force. This load cell, with a maximum load of 1 ton, is a force transducer for the measurement of static and dynamic loads in compression and tension. This equipment, was manufactured by AEP transducers and provided by CEiiA. For data collection a WIMOD transmitter and WISTAR receiver were used. The WIMOD transmitter, applied on the body of the load cell, through a wireless communication integrated interface with WISTAR receiver, shown in Appendix D. This receiver had a DATALOGGER option which allows to memorize measurements and to keep them in the internal memory. WIMOD can also communicate directly in real time to a Personal Computer (PC) which uses a software for instant data collection. However, this faster process was unavailable. So, for data collection the DATALOGGER option was used. The WISTAR was configured accordingly the needs (recording time, transmission frequency, bound rate and time between each communication). Further, since the calibration of these instruments is done periodically, the author only set zero at the desired position (initial position). This equipment had an improved uncertainty from 0.005% to 0.02% [61].

4.2.2 Weight difference

A study of weight difference between all combinations was made before the Experimental Tests. After some testing runs, it was revealed that this study was also important and had influence on the results due to the friction force between the wheels and the rails, which depends on the weight of the towing carriage (trolley, assembly and model test). This study consisted in: measuring the Volume (V) of all the body's components precisely using CATIA V5R24 software; use the Archimedes' Principle ("indicates that the upward buoyancy force that is exerted on a body immersed in a fluid, whether fully or partially submerged, is equal to the weight of the fluid that the body displaces" [62]) to calculate the Buoyancy (B) of each component (shown in Table 4.6 & Table 4.7) and define the heaviest combination as standard (Table 4.8); calculate the difference between the standard (heaviest) combination and each

other; and get an approximation of weight necessary to be added for each combination (Table 4.9).

Table 4.6 - Nose characteristics with buoyancy.

Nose	L [mm]	m [g]	V [mm^3]	B [g]	Wetted mass [g]
E1	64	633.0	222068.7	222.1	411.0
E2	128	1244.0	436534.8	436.5	808.0
E3	192	1855.0	651000.8	651.0	1204.0

Table 4.7 - Tail characteristics with buoyancy.

Tail	L [mm]	m [g]	V [mm^3]	B [g]	Wetted mass [g]
E1	128	1244.0	436534.8	436.5	808.0
E2	192	1855.0	651000.8	651.0	1204.0
E3	256	2467.0	865466.9	865.5	1601.0
C1	128	820.0	287766.1	287.8	532.0
C2	192	1283.0	450256.0	450.3	833.0
C3	256	1775.0	622878.0	622.9	1152.0

Table 4.8 - Mass Combinations.

Combination 1	Combination 7	Combination 13
E1 + E1 (g) 1218	E2 + E1 (g) 1615	E3 + E1 (g) 2012
Combination 2	**Combination 8**	**Combination 14**
E1 + E2 (g) 1615	E2 + E2 (g) 2012	E3 + E2 (g) 2409
Combination 3	**Combination 9**	**Combination 15**
E1 + E3 (g) 2012	E2 + E3 (g) 2409	E3 + E3 (g) 2805
Combination 4	**Combination 10**	**Combination 16**
E1 + C1 (g) 943	E2 + C1 (g) 1340	E3 + C1 (g) 1737
Combination 5	**Combination 11**	**Combination 17**
E1 + C2 (g) 1244	E2 + C2 (g) 1641	E3 + C2 (g) 2037
Combination 6	**Combination 12**	**Combination 18**
E1 + C3 (g) 1563	E2 + C3 (g) 1960	E3 + C3 (g) 2357

Table 4.9 - Combinations weight with its adding load values.

Same combinations		Comb. Value [g]	Adding load [g]	Adding load (aprox. 50g)	Error %
Group 1	3;8;13	2012	794	800	0.8
Group 2	2;7	1615	1190	1200	0.8
Group 3	1	1218	1587	1600	0.8
Group 4	5	1244	1562	1550	0.7
Group 5	4	943	1862	1850	0.7
Group 6	**15**	**2805**	**0**	**STANDARD**	**0.0**
Group 7	6	1563	1242	1250	0.6
Group 8	9	2409	397	400	0.8
Group 9	10	1340	1466	1450	1.1
Group 10	11	1641	1165	1150	1.3
Group 11	12	1960	846	850	0.5
Group 12	14	2409	397	400	0.8
Group 13	16	1737	1069	1050	1.8
Group 14	17	2037	768	750	2.4
Group 15	18	2357	449	450	0.3

As shown on Table 4.6 to Table 4.9, some combinations have the same weight. Thus, the author organized the combinations into Groups. Since it was not possible to add the exact value of load, the author also made an estimation about the error using an approximation of adding load. The maximum value for this error is 2.4% (Table 4.9), which has negligible influence. Images of this consideration are shown in Appendix E.

4.2.3 Drag Calculation

As shown before, the model was connected to the metallic structure (attached to the towing tank) through two struts covered by fairings. However, the load cell was connected to the towing carriage, measuring the total resistance force of all sets. In order to measure only the AUV's resistance force, the method adopted was the same of Mansoorzadeh and Javanmard [52] adopted for their experiment. The method is to measure only the resistance force of towing carriage with the metallic structure and struts attached. Then, measure the resistance force of all components (towing carriage, metallic structure, struts and AUV model). Finally, subtracting these two processes, the AUV's resistance force could be calculated. The method implemented for Drag estimation is shown in Figure 4.10.

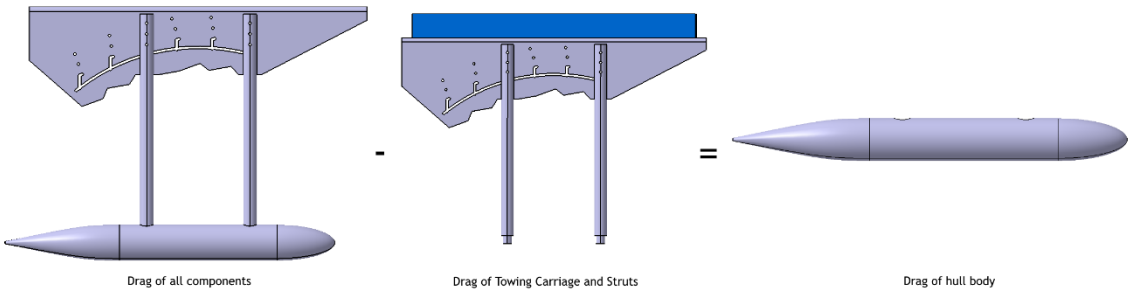

Figure 4.10 – Procedure adopted to calculate the Drag caused, exclusively, by the hull body.

4.2.4 Frequency inverter study / Velocity estimation

On this section, considerations to estimate the AUV's velocity will be detailed. As will be shown here, the velocity is directly linked with the frequency inverter, i.e. the frequency inverter controls the three-phase motor frequency.

As described previously, the frequency inverter can operate up to 50 Hz. The methodology adopted to find the velocity in which the AUV model was travelling was: Define a known distance to measure the time which AUV model takes to run; save that time and frequency; using the Equation (4.2) calculate the velocity; and repeat this process until discover the maximum velocity desired.

$$U = \frac{d}{t} \tag{4.2}$$

Where U is the velocity, d the distance traveled in meters (m) and t the time in seconds (s).

The Table 4.10 demonstrates all these considerations above referred.

Table 4.10 – Corresponding Velocity for each Frequency. Elliptic Nose 192mm – Elliptic Tail 256mm, distance 4.48m.

Frequency [Hz]	Time collection [s]					Average time [s]	Velocity [m/s]
	1st	2nd	3rd	4th	5th		
4	21.57	21.69	21.90	22.13	21.97	21.85	0.21
5	17.34	17.03	17.22	17.15	17.16	17.18	0.26
6	14.06	13.97	14.00	13.94	13.90	13.97	0.32
7	11.72	11.72	11.75	11.81	11.59	11.72	0.38
8	10.12	10.06	10.16	10.06	10.09	10.10	0.44
9	**8.90**	**8.97**	**8.84**	**8.87**	**8.91**	**8.90**	**0.50**
10	8.03	8.00	7.91	8.00	7.97	7.98	0.56
11	7.19	7.28	7.22	7.25	7.19	7.23	0.62
12	6.62	6.53	6.53	6.75	6.56	6.60	0.68
13	**6.03**	**6.06**	**6.06**	**6.09**	**6.06**	**6.06**	**0.74**
14	5.62	5.78	5.63	5.59	5.62	5.65	0.79
15	5.19	5.21	5.25	5.28	5.25	5.24	0.86
16	4.87	4.94	4.94	4.84	4.84	4.89	0.92
17	**4.56**	**4.53**	**4.56**	**4.66**	**4.56**	**4.57**	**0.98**
18	4.21	4.28	4.37	4.31	4.25	4.28	1.05

The distance measured was 4.48 m, located at the mid-section of the towing tank. The time collection was repeated five times for each case, in order to obtain a more reliable time. The Frequency tested was between 1 and 20 Hz. However, a frequency lower than 4 Hz had no sufficient Torque to pull the towing carriage. It was also verified that for frequencies above 18 Hz the towing carriage could not stop in a safety mode. The velocities and frequencies chosen are marked in Table 4.10.

Froude number verification according velocities

Once the velocities were defined, the Froude number verification is important to understand which condition should be respected for fully submerged condition, according to the Figure 2.10.

Following the Equation (2.12), the Froude number for maximum length combination (800mm) and for 0.5, 0.75 and 1.00 m/s are given, respectively, by (Equation (4.3), (4.4) and (4.5)),

$$Fn\ (0.5) = \frac{0.5}{\sqrt{9.81\ .\ 0.8}} \cong 0.179 \tag{4.3}$$

$$Fn\ (0.75) = \frac{0.75}{\sqrt{9.81\ .\ 0.8}} \cong 0.268 \tag{4.4}$$

$$Fn\ (1.00) = \frac{1.00}{\sqrt{9.81\ .\ 0.8}} \cong 0.359 \tag{4.5}$$

As demonstrated by these Equations, operating in a low Froude number (Fn < 0.5), the fully submerged condition is accepted, according Figure 2.10 ($H^* = 2.8$), and fully respect all the different conditions considered. Even for sections of the tank where the depth of the tank is smaller this condition is respected, $h = 0.25$ (Equation (4.6)).

$$H^* = \frac{0.25}{0.08} = 3.125 \tag{4.6}$$

4.3 Experimental Tests Results

After all considerations referred above, the Experimental Tests were performed. However, due to some technical issues, it was not possible to run all combinations. Thus, at least eleven from eighteen combinations were performed (around 1100 test). In order to achieve the optimum configuration and its conditions, several studies were done and will be shown below. The author opted to look for a trend between the results, since there are a considerable number of them. These results are structured in a coherent manner: find the optimum configuration for each tail shape, compare them between each other, and finally demonstrate a detailed study of the optimum configuration. Should be noted that by the lack of some results, including results for the biggest nose (N/D = 2.4), it was not possible to display results for this ratio.

4.3.1 Length Optimization (Conical Tail)

For this Conical Tail study, two steps were considered in order to find the effect of AoA and Velocity, on Drag. These steps include the nominal AoA and velocity for this AUV model. The first step is: by fixing the AoA at 0 degrees, finding the optimum nose and tail configuration. Consecutively, the second one is: by fixing the velocity at 1 m/s, finding the optimum nose and tail configuration.

Influence of Nose length on Drag for nominal AoA (0 degrees)

Fixing the AoA at 0 degrees and T/D at 3.2, varying the N/D within a range of 0.8 to 1.6, Drag Results are shown in Chart 4.1:

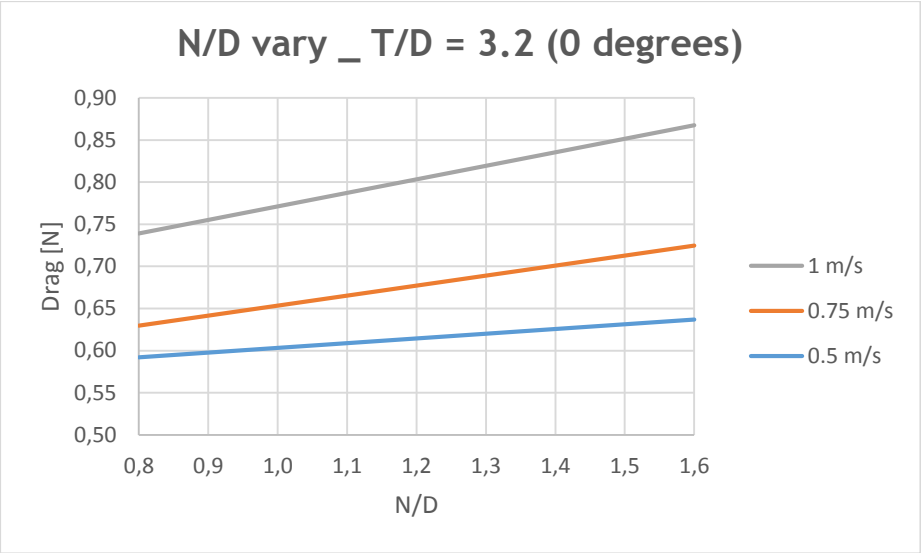

Chart 4.1 – Drag Results for different velocities operating at 0 degrees, varying N/D between 0.8 to 1.6, and fixing the T/D = 3.2.

The Chart 4.1 demonstrates a trend of all velocities for the optimum N/D ratio at 0.8. It can be noted that Drag increases linearly with the increase of N/D ratios. Also, Drag increases whenever the velocity increase. There is a Drag difference between 0.75 and 1.00 m/s that is nearly the double compared with 0.50 and 0.75 m/s.

Influence of Tail length on Drag for nominal AoA (0 degrees)

Fixing the AoA at 0 degrees and N/D at 0.8, varying the T/D within a range of 1.6 to 3.2, the Drag results are shown in Chart 4.2:

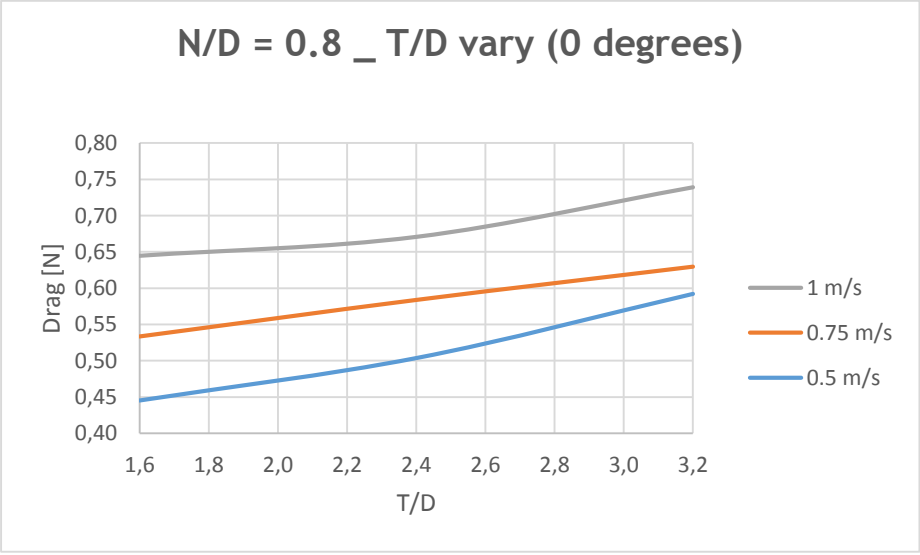

Chart 4.2 - Drag Results for different velocities operating at 0 degrees, fixing N/D and varying T/D between 1.6 to 3.2.

The Chart 4.2 presents an optimum T/D ratio at 1.6. For T/D = 1.6, the Drag difference between each velocity it is nearly close until T/D = 2.4. This Chart also denote higher Drag for higher velocities. Furthermore, Drag increases non-linear with T/D ratios.

Influence of Nose length on Drag for nominal velocity (1 m/s)

Fixing the velocity at 1 m/s and T/D at 3.2, varying the N/D within a range of 0.8 to 1.6, the Drag results are shown in Chart 4.3:

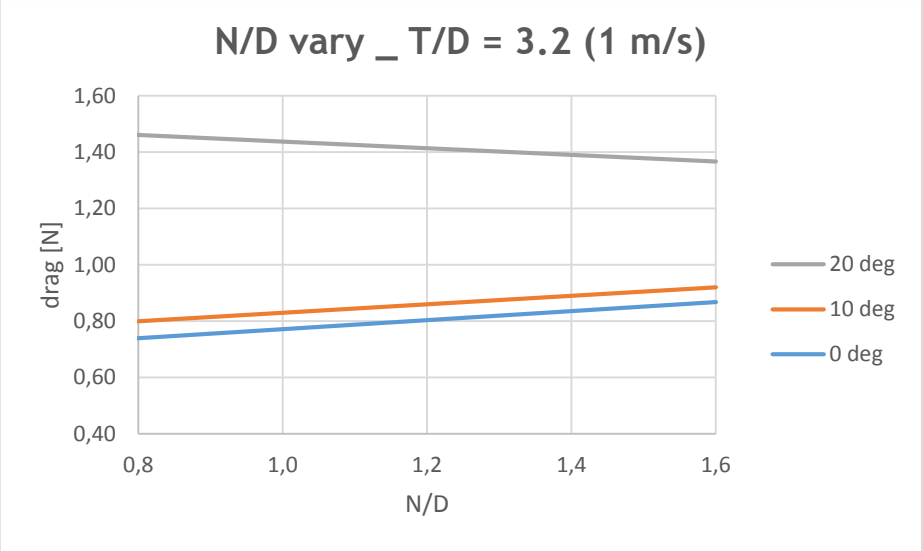

Chart 4.3 - Drag Results for different AoA's operating at 1 m/s, varying N/D between 0.8 to 1.6, and fixing the T/D = 3.2.

The Chart 4.3 shows that Drag increases with the increase of N/D ratio at 0 and 10 degrees, and between both. Further, for these AoA's the optimum N/D ratio is 0.8. However, for an AoA of 20 degrees, the Drag decreases by increasing the N/D ratio. The optimum N/D ratio for this AoA is 1.6. This occurrence can be justified with the experimental error associated with high velocities, AoA's and for bigger lengths (high N/D ratio, in this case). AUV model operating under these conditions might bring into consideration the Wall and Surface effects, albeit dimensions are being respected according literature review [24]. Globally, the optimum N/D ratio can be considered 0.8 (operating under nominal velocity the AUV should operate with low AoA's). At this N/D ratio, the Drag value almost double up between 0 and 20 degrees.

Influence of Tail length on Drag for nominal velocity (1 m/s)

Fixing the velocity at 1 m/s and N/D at 0.8, varying the T/D within a range of 1.6 to 3.2, the Drag results are shown in Chart 4.4:

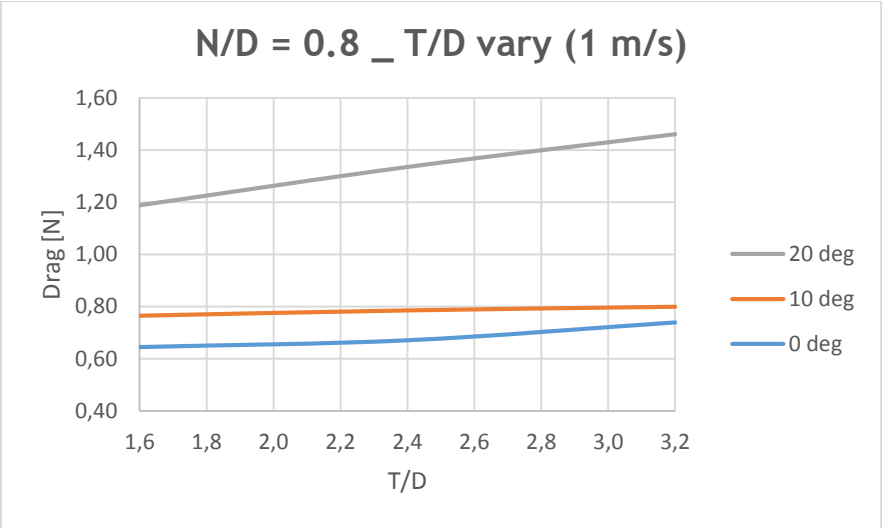

Chart 4.4 - Drag Results for different AoA's operating at 1 m/s, fixing N/D and varying the T/D between 1.6 to 3.2.

The Chart 4.4 indicates an optimum T/D ratio of 1.6. At this T/D ratio, the Drag value almost double up between 0 and 20 degrees. For lower AoA's the Drag almost remains constant for different T/D ratio. However, for an AoA of 20 degrees Drag has a considerable increase with the increase of T/D ratio.

4.3.2 Length Optimization (Elliptical Tail)

Following the same procedure applied for Conical Tail, a parallel Elliptical Tail study was made find the effect of AoA and Velocity on Drag, to finally compare both shapes later.

Influence of Nose length on Drag for nominal AoA (0 degrees)

Fixing the AoA at 0 degrees and T/D at 3.2, varying the N/D within a range of 0.8 to 2.4, the Drag results are shown in Chart 4.5:

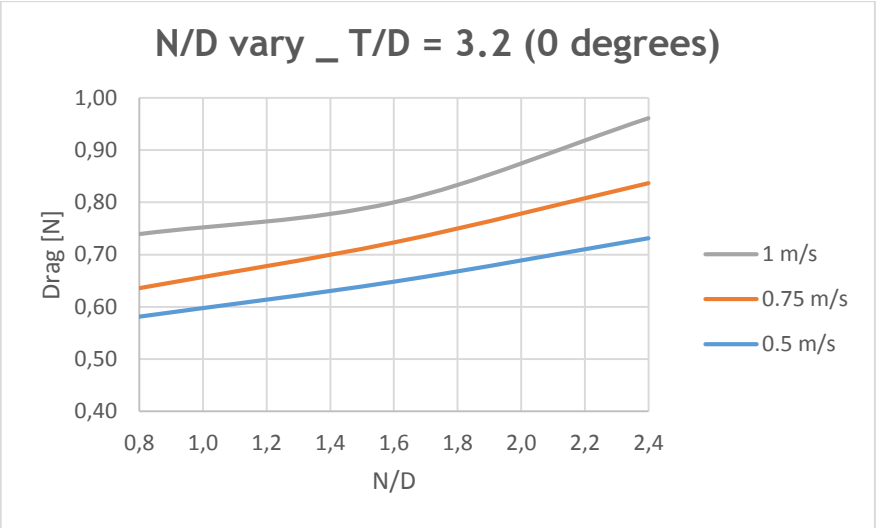

Chart 4.5 - Drag Results for different velocities operating at 0 degrees, varying N/D between 0.8 to 2.4, and fixing the T/D = 3.2.

The Chart 4.5 presents an optimum N/D ratio of 0.8. Drag increases with velocity and have the same behavior for N/D ratio. For higher N/D = 1.6, Drag difference between each velocity tends to increase.

Influence of Tail length on Drag for nominal AoA (0 degrees)

Fixing the AoA at 0 degrees and N/D at 0.8, varying the T/D within a range of 1.6 to 3.2, Drag's results are shown in Chart 4.6:

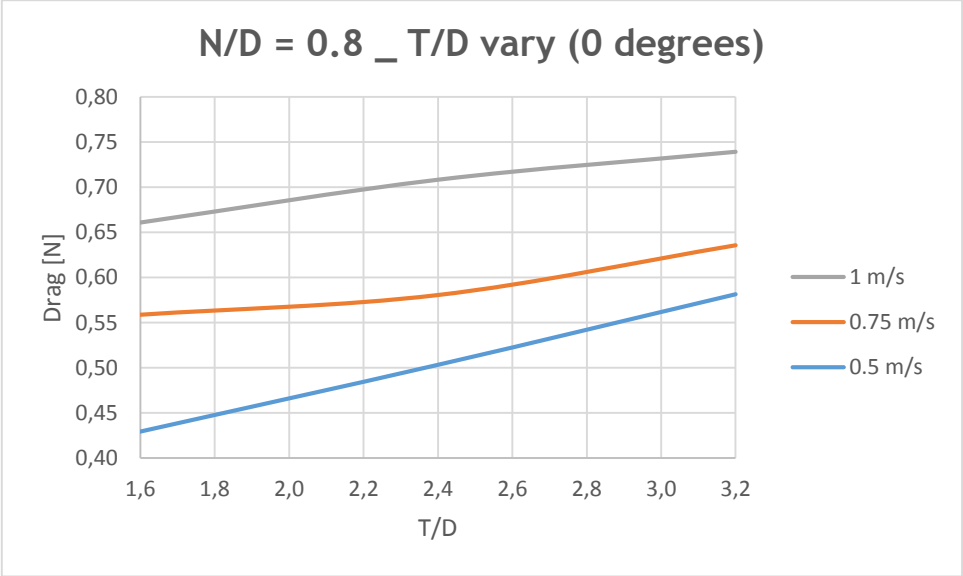

Chart 4.6 - Drag Results for different velocities operating at 0 degrees, fixing N/D and varying T/D between 1.6 to 3.2.

The Chart 4.6 demonstrates an optimum T/D ratio of 1.6. Drag increases with the increase of velocity. The Drag difference between the velocities 0.5 and 1 m/s are smaller with the increase of T/D ratio. Further, Drag also increases with the increase of T/D ratio.

Influence of Nose length on Drag for nominal velocity (1 m/s)

Fixing the velocity at 1 m/s and T/D at 3.2, varying the N/D within a range of 0.8 to 2.4, the Drag results are shown in Chart 4.7:

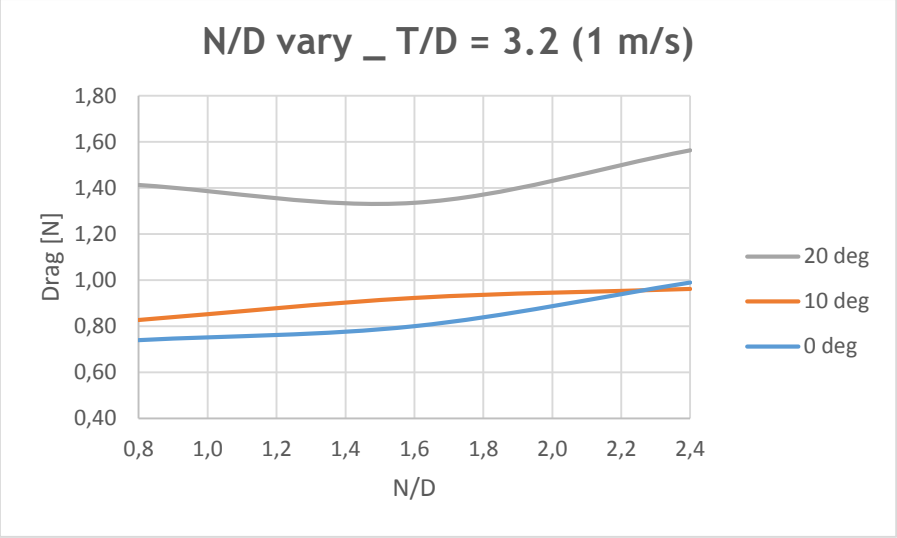

Chart 4.7 - Drag Results for different AoA's operating at 1 m/s, varying N/D between 0.8 to 2.4, and fixing the T/D = 3.2.

The Chart 4.7 denotes that Drag increases for AoA's of 0 and 10 degrees. Furthermore, for these AoA's the optimum N/D ratio is 0.8. However, for an AoA of 20 degrees, the Drag decreases by increasing the N/D ratio until N/D = 1.6, which is the optimum N/D ratio for this AoA, and increases hereafter. This behavior can be justified with the experimental error associated with high velocities, AoA's and for bigger lengths. AUV model operating under these conditions might bring into consideration the Wall and Surface effects, as referred previously. Globally, the optimum N/D ratio can be considered 0.8 (operating under nominal velocity the AUV should operate with low AoA's). At this N/D ratio, the Drag value almost double up between 0 and 20 degrees of AoA.

Influence of Tail length for nominal velocity (1 m/s)

Fixing the velocity at 1 m/s and N/D at 0.8, varying the T/D within a range of 1.6 to 3.2, the Drag results are shown in Chart 4.8:

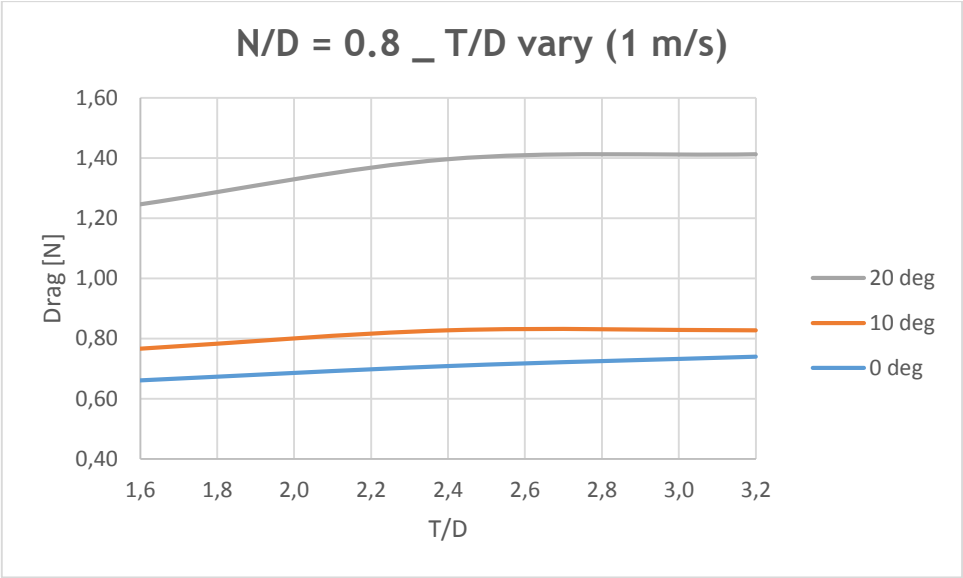

Chart 4.8 - Drag Results for different AoA's operating at 1 m/s, fixing N/D and varying T/D between 1.6 to 3.2

The Chart 4.8 shows an optimum T/D ratio at 1.6. At nominal AoA (0 degrees), Drag increases linearly with the increase of T/D ratio. For bigger AoA's, Drag increases with the increase of T/D until 2.4. Hereinafter, Drag has the trend to remain constant.

4.3.3 Tendencies

Analyzing the Charts presented above, there is clearly a common trend between both cases (Elliptical and Conical). However, it is not clear which of these cases is the optimum. Some conclusions should be made in order to compare them afterwards.

For 0 degrees, a N/D ratio of 0.8 was the optimum value for both Conical and Elliptical tails. Further, Drag's behavior in these cases, is almost the same (increases with regard to Velocity and AoA).

For 0 degrees, a T/D ratio of 1.6 is clearly the optimum value for both tail shapes. Drag also increase with the increase of T/D ratios and Velocity.

Relatively to the nominal velocity (1 m/s), both Charts (Chart 4.3 and Chart 4.7) (Elliptical and Conical, respectively) describe the same behavior until N/D = 1.6, showing that there is a trend between both combinations, being interesting to note the similar behavior of these Charts. N/D ratio of 0.8 seem to be the optimum value for both cases, although for an AoA of 20 degrees the optimum value is N/D = 1.6. Drag for N/D ratio of 0.8 almost doubles up for both cases, since 0 degrees to 20 degrees of AoA.

Finally, at the velocity of 1 m/s, the optimum T/D ratio is 1.6 for Elliptical and Conical (Chart 4.4 and Chart 4.8, respectively) tails. In these cases, Drag has a similar behavior for 0 and 10 degrees of AoA. Furthermore, for 20 degrees of AoA, the behavior is also similar until T/D ratio of 2.4.

4.3.4 Comparison between optimum configurations

After careful analysis, it has been concluded that for both cases the optimum configuration is N/D = 0.8 (elliptical nose) and T/D = 1.6 (elliptical and conical tail). Following the study, the optimum configuration between both cases should be found. The Chart 4.9 and Chart 4.10 compare both cases, Conical and Elliptical to find the tail shape that produces lower Drag by varying AoA and Velocity, respectively.

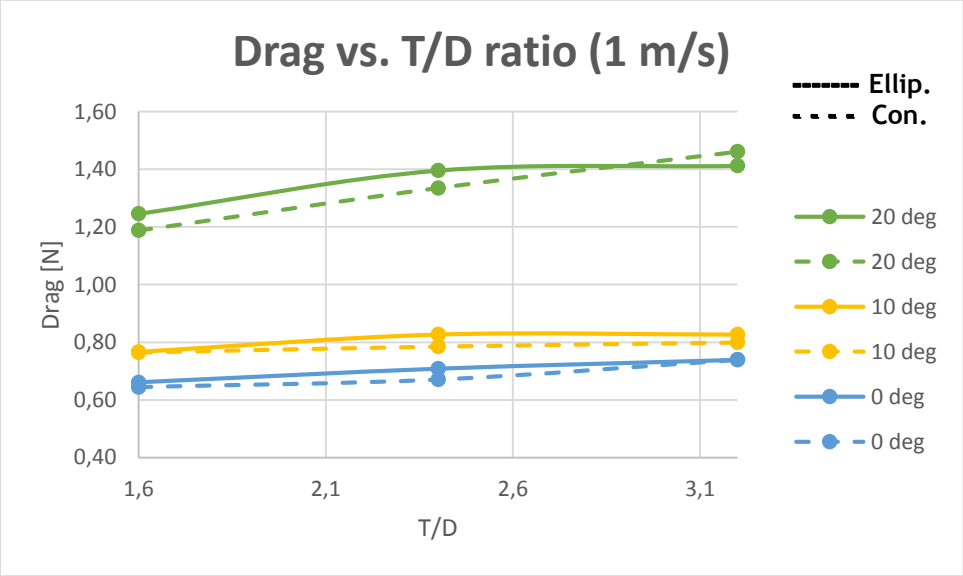

Chart 4.9 - Comparison of Drag Results between Conical and Elliptical tail shapes, for different AoA's on a velocity of 1 m/s. FALTA LEGENDAR CORRECTAMENTE

The Chart 4.9 shows the comparison between an Elliptical and Conical Tail shapes operating under the same conditions, i.e. operating at 1 m/s for different AoA's (0-20°). Although tail shapes demonstrate a similar result, the Conical tail shape shows to be the geometry that produce lower Drag.

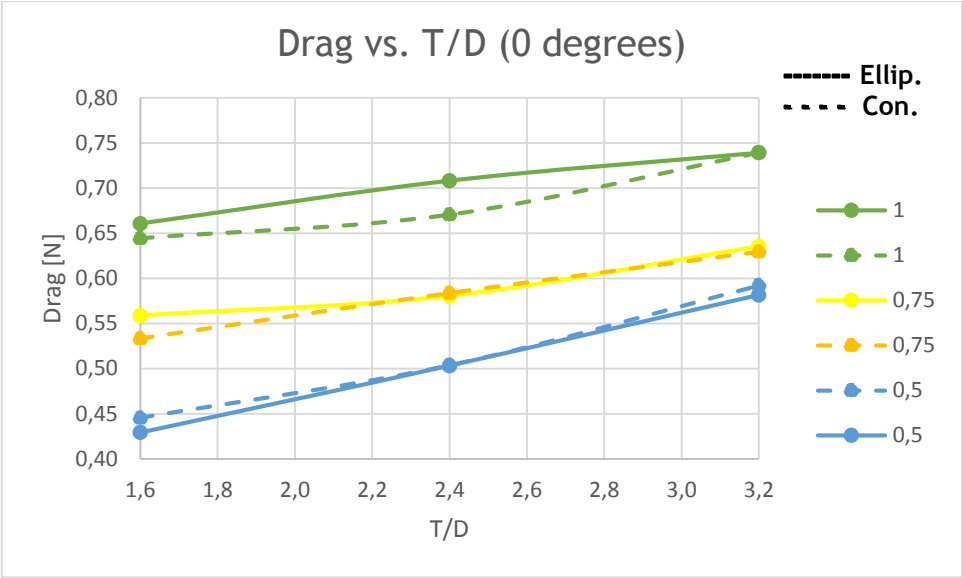

Chart 4.10 - Comparison between Elliptical and Conical tail shapes, for different velocities at 0 degrees of AoA.

The Chart 4.10 demonstrates the comparison between Elliptical and Conical tail shapes operating at different velocities on a fixed AoA (0 degrees). There are also similar results for both cases, but for nominal velocity (1 m/s) it is evident that Conical Tail shape shows to be the final optimum configuration. Therefore, based on these two comparisons showed, the author will focus on the optimum geometry for a more detailed study.

4.3.5 Optimum Experimental Combination

As described previously, a combination of an Elliptical nose with a N/D = 0.8 and a Conical tail with a T/D = 1.6 showed to be the optimum configuration. Thus, it will be showed Drag force and Coefficient variation with Velocity and AoA. The two following Charts (Chart 4.11 & Chart 4.12) exhibit a study of Drag force and Coefficient, respectively, for the optimum combination.

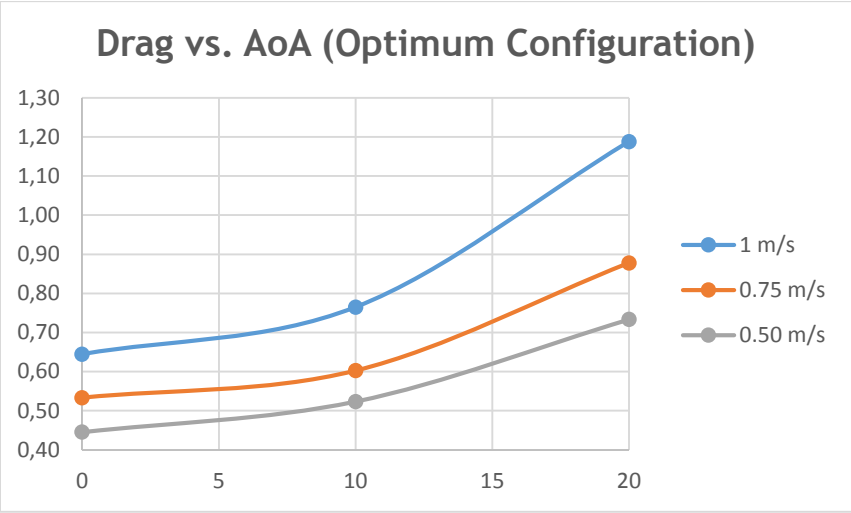

Chart 4.11 - The influence of AoA's (0 - 20˚) on Drag, for different velocities (0.5 - 1.00 m/s).

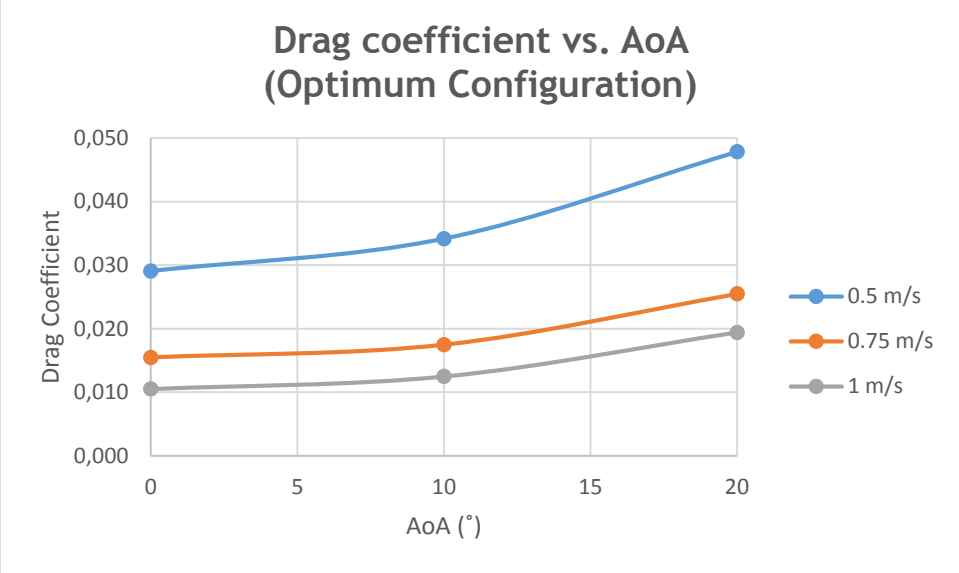

Chart 4.12 - The influence of Velocity (0.5 – 1.00 m/s) on Drag, for different AoA's (0 - 20˚).

Analyzing these two Charts (Chart 4.11 & Chart 4.12) represented above, it can be concluded that the Drag increases with Velocity and AoA. Relatively to nominal conditions (1 m/s and 0 degrees), it can be also concluded that Drag is always minimum when operating at 0 degrees for all velocities. However, operating at 1 m/s, Drag is higher comparatively to lower velocities. There is an operating point that should be avoided, in which Drag reaches its maximum. This point is: Velocity = 1 m/s and AoA = 20˚. Drag Coefficient increases with the increasing of AoA, and decreases with the increasing of velocity. Thus, can be concluded that the influence of AoA on Drag is higher for greater velocities.

Chapter 5

5 Numerical Analysis

This section demonstrates the steps and choices made, in order to validate the Numerical Simulation against the Experimental Procedure. This procedure embraces the Model's dimensions intended to be studied initially, i.e. the hull's dimensions applied for Numerical Simulation are shown in Figure 3.1. The CFD software ANSYS FLUENT 16.0 was used for this thesis to predict the hydrodynamic coefficients and forces. Thus, Numerical Results and conclusions about Numerical Procedure will be also provided.

5.1 Numerical Setup (Procedure)

This procedure comprises the use of ANSYS WorkBench (WB) 16.1, ANSYS Meshing 16.1 and ANSYS FLUENT 16.1 that were used on this thesis. A Fluid Flow (FLUENT) template was chosen to start this procedure (default Analysis System), which includes a sequence of steps as: Geometry, Mesh, Setup, Solution and Results.

5.1.1 Model Design and Flow Domain

Following the sequence referred above, the Geometry was designed using the CATIA V5R24. The Geometry was imported to the WB in a file format Computer-Aided Design (CAD). To define the Flow Domain, a Control Volume (CV) was also created. There are no exact guideline values regarding the dimensions of this CV, although several authors [11], [52], [57], [63] refer that the solution domain needs to be large enough to capture the entire wake development. Therefore, the CV dimensions were chosen to ensure that all interactions and wake developments were captured. The Figure 5.1 shows the Fluid Domain dimensions used for this Numerical Simulation.

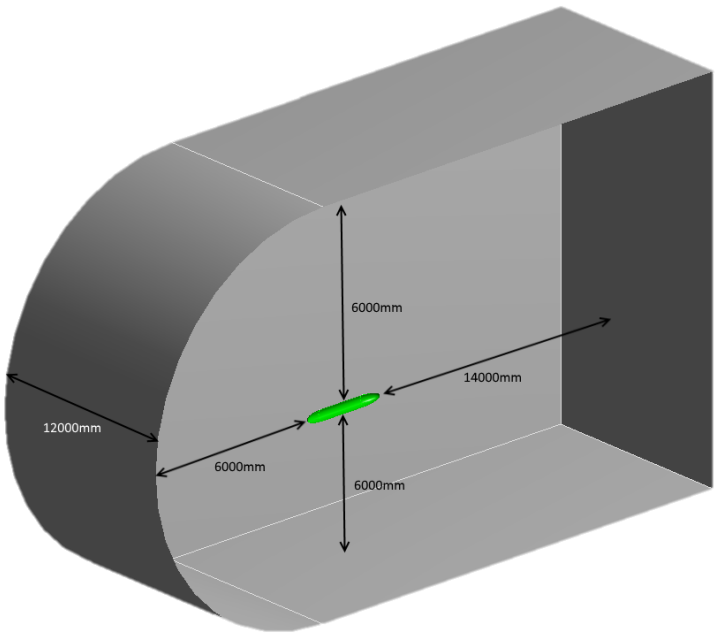

Figure 5.1 - Control Volume dimensions.

The hull dimensions (Diameter of 340 mm and mid-body length of 1500 mm) used to function comparatively as base for CV dimensions. However, in this case it was not applied, since the literature review varies too much to define a precise value which guarantees that the flow is not affected due to small dimensions of CV [11], [52], [57], [63].

The front of the CV is semi-circular, as demonstrated in Figure 5.1. Due to a more complex calculus (higher computational cost) with relative velocity passing by the corners when operating at high AoA, this configuration was adopted to simplify the process, improve mesh quality and help with results convergence.

Since the CV is only relative to the flow field, the hull body was removed from the CV, to apply all fluid parameters/conditions in the CV, i.e. the CV must be occupied only with fluid, the body's volume must be extracted.

5.1.2 Meshing Process

After defining the Fluid Domain, the division of the flow into small elements must be done. The software ANSYS Meshing was used to do this decomposition. During the Meshing Process, there are several important parameters which influence the Numerical Simulation Results, as domain size, mesh size and distance of the first layer of the cells to the hull (y), controlled by the Inflation Layer. This distance introduces to y^+ parameter. y^+ is the dimensionless number from the body's surface to the near wall node and it is given by the Equation (5.1),

$$y^+ = \frac{y.\mu^*}{\nu} \tag{5.1}$$

Where y is the distance of the first layer of the cells to the hull, μ^* the friction velocity and ν the local kinematic viscosity of the fluid.

The friction velocity (μ^*) can be expressed as (Equation (5.2)),

$$\mu^* = \sqrt{\frac{\tau_W}{\rho}} \tag{5.2}$$

Where τ_W is the shear stress and ρ the density.

Turbulent flows are considerably affected by the presence of walls. So, an accurate representation of the flow in the near-wall region gives a better prediction of wall-bounded turbulent flows. Thereby, depending on each Turbulence Model and Near-Wall Treatment, there is a range of optimum values for y^+ where the reliability of numerical solutions is improved, i.e. controlling the Inflation Layer, the y^+ can be adjusted into this range. For κ-ε turbulence model, the calculation of the boundary layer is substituted by a wall function reducing this way the computational requirements. Nevertheless, the use of these wall functions can only be performed if the value of y^+ is between 30 and 300.[42].

In order to optimize the Meshing Results as much as possible, several parameters were tested to understand how their influence on results. The input parameters tested are shown in Table 5.1. Thus, the output parameters as Cell number y^+ are also shown in Table 5.1. Several other Meshing tests were made, however only the most relevant are shown below.

Table 5.1 - Several Meshing parameters tested.

Auv faces	**Element size**	0.01	0.01	0.01	0.02	0.007	0.007	0.006	0.005	0.004	0.003
	Curv normal angle	10	10	10	5	10	5	5	10	10	10
	Growth rate	1.15	1.1	1.1	1.1	1.1	1.1	1.1	1.1	1.1	1.1
	min size	0.0005	0.0004	0.0003	0.0002	0.0004	0.0002	0.0003	0.0003	0.0002	0.0002
wake	**Element size**	0.1	0.1	0.06	0.06	0.06	0.06	0.06	0.06	0.05	0.04
Mesh	**Growth rate**	1.2	1.2	1.2	1.2	1.2	1.2	1.15	1.15	1.15	1.15
Inflation layer	**First cell height**	0.003	0.002	0.0015	0.0015	0.002	0.0015	0.002	0.002	0.0015	0.0015
	Number of layers	5	5	5	5	5	5	5	5	5	5
	Growth rate	1.2	1.15	1.15	1.15	1.15	1.15	1.15	1.15	1.15	1.15
Output parameters	**Cell No (tetra)**	1796895	2311103	2464303	1817579	4023766	3990712	4911547	6620161	9629189	15785430
	Cell No (poly)	419260	504798	530643	370622	905507	900812	1136846	1568379	2309891	3864672
	Y+ (min)										
	Y+(85% cells)	40-80	34-55	25-35	25-35	25-36		35-45		28-36	25-40
	Y+ average (85% cells)	60	40	30	30	30		40		31	28
	Y+ (max)	80	53	40	40	40		55		42	42

Applied exclusively on Hull faces, the input parameters modified during several attempts were: Element size, Curvature Normal Angle, Growth Rate and Minimum size of an element.

The Element size specifies the element size used for the specific selection, in this case, to Hull faces. The Curvature Normal Angle is the maximum angle that one element edge is allowed to span. Growth Rate represents the increase between succeeding layer elements. The Minimum size of an element represents the minimum size that is allowed to elements for the specific selection [64].

The Wake section is a volume created to add a specific refinement at the desired location. This Wake is represented in Figure 5.2.

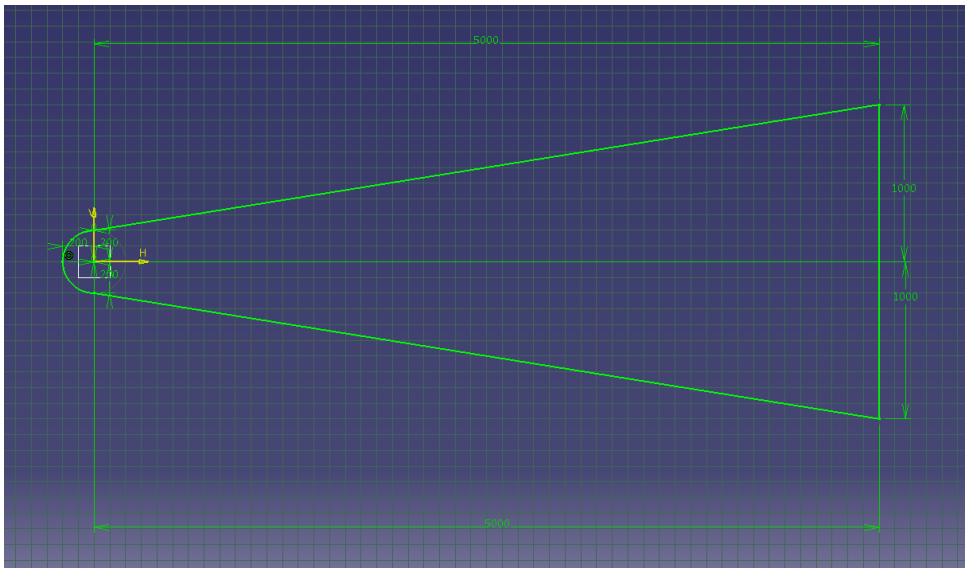

Figure 5.2 - Shape of the Wake for an improved Mesh treatment.

As can be seen in Figure 5.2, the Wake's shape was chosen to improve the mesh refinement on a specific location where the Wake development is crucial. The Element size was adjusted to understand how important was the mesh treatment on that location.

The Mesh section refers to the Mesh in general. Elements not selected for a specific treatment, will follow the condition imposed by Mesh section. It is important to defined the Maximum Element Size in a far field and its Growth Rate, as shown in Table 5.1.

The Inflation Layer, that includes the parameters First cell height, Number of layers and Growth Rate, represents the Boundary Layer. This is a crucial section to the Meshing Process. The boundary layer height should be predicted by empirical methods and then similar represented at Inflation Layer. Details about Boundary Layer can be seen in reference [32].

The Meshing Results are shown in Figure 5.3. The Mesh domain was converted from Tetrahedral Mesh to Polyhedral Mesh, since Polyhedral Mesh requires a smaller computational cost and keep showing good Results by improving the Mesh quality.

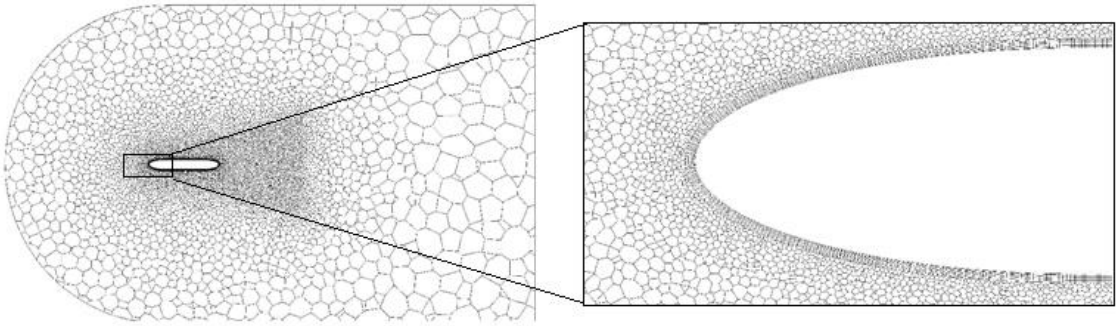

Figure 5.3 - Left) Mesh Result; Right) Detailed Nose Mesh Result.

Figure 5.3 presents the Mesh Result with a refinement on Body Wake (Figure 5.3 - Left). This Result had nearly 1 million Polyhedral cells, and the range of y^+ was between 35 and 45 (Table 5.1, grey column). Furthermore, the Inflation Layer can be also seen (Figure 5.3 - Right) with an improved refinement with comparison to the entire Mesh. Knowing that the y^+ for Standard κ-ε Turbulence Model (used on Figure 5.3) should be close but above 30 and bellow 300, these values are quite acceptable.

5.1.3 Physical Model Setup and Simulation

Fluid properties

The liquid water was chosen as fluid. The fluid properties are shown in Table 5.2.

Table 5.2 - Fluid properties.

Density	1027 [kg/m^3]
Viscosity	0.00167 [kg/(s.m)]

Boundary Conditions

To define several parameters at Fluid Domain, the boundary conditions were specified. The Sidewalls of the CV, corresponding to far-field flow, were defined as symmetry plane to highly reduce the CPU cost on those boundaries. The hull body was defined with a Stationary wall condition (no-slip condition). The velocity inlet boundary condition was applied at the Inlet. Pressure-outlet boundary condition was applied at outlet.

The flow velocities were set and changed at velocity inlet boundary condition. The flow direction was decomposed when a specific AoA was desired. Thus, turbulence quantities were

also set. Since the simulations were compared with experimental towing tank tests, the turbulence intensity was set to be 0.05% and the turbulence length was equal to 7% of the hull body length (Dantas & Barros, 2013).

The convergence criteria adopted for this Numerical Simulation was 10-5 in residuals.

Two Turbulence Models were chosen for the Numerical Simulations: Standard κ-ε and κ-ω SST models. A mesh-independent study was also made to evaluate which Turbulence Model was chosen, following a mesh-quality/computational cost trade-off. The Chart 5.1 demonstrates this study. Two empirical methods were also implemented to compare against the Turbulence Models. These empirical methods were G&J and VT methods applied by Alam et al. [36] on their study.

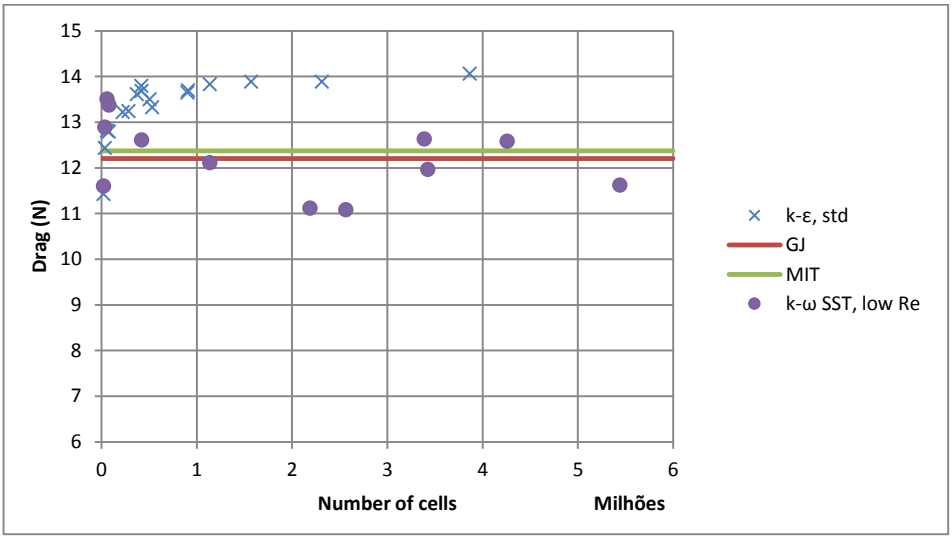

Chart 5.1 - Mesh-independency study (referent to Table 5.1).

As can be seen in Chart 5.1, the Standard κ-ε Turbulence Model requires a lower computational cost when compared to the κ-ω SST Model to stabilize, i.e. Standard κ-ε Turbulence Model better predicts Drag value for lower computational cost, while the Drag value do not stabilize for κ-ω SST Model, not even using higher computational cost. Consequently, the Standard κ-ε was the Turbulence Model adopted.

5.2 Numerical Validation

In order to validate the Numerical Simulations against the Experimental Tests, a pertinent procedure was adopted. Following the Experimental Test Results used in Chapter 4, the comparison Numerical/Experimental was made. Therefore, the N/D ratio was fixed at 0.8 (optimum Experimental Nose length) and the T/D ratio varied between 1.6 and 3.2, for each specific Tail shape (Elliptical and Conical) and then comparing the Experimental Tests with Numerical Simulations. However, due to the scale difference between each Procedure

(Experimental and Numerical), the Reynold's similarity was applied to guarantee similar flow conditions. However, it was not possible to apply the Equations (2.7) and (2.8), since these Equations assume the same fluid properties in both cases. Therefore, Table 5.3 shows the Reynold's similarity done, considering different flow properties.

Table 5.3 – Reynold's Similarity applied.

	Experimental Model	Full-scale Prototype	Re %Approx.
Density (ϱ) [kg/m3]	996,78	1027,00	-
Viscosity (v) [kg/(s.m)]	0,00085	0,00167	-
Length (L) [m]	0,544	2,316	-
Velocity (V) [m/s]	1,00	0,45	-
Reynold's Number (Re)	638773	640922	0,3

As can be seen in Table 5.3, to assume the similar Reynold's number for Experimental model and full-scale prototype, these conditions showed must be respected. To achieve similar flow conditions for the experimental model travelling at 1 m/s, the full-scale prototype should be tested for a velocity of 0.45 m/s (see Table 5.3). The Reynold's number it is not the same for both cases, but as demonstrated the Error is so small (0.3%), that it is assumed equal Reynold's numbers to achieve a desired operational velocity of the full-scale prototype.

Consequently, the Chart 5.2 & Chart 5.3 demonstrates this study for an Elliptical and Conical Tail shapes, respectively.

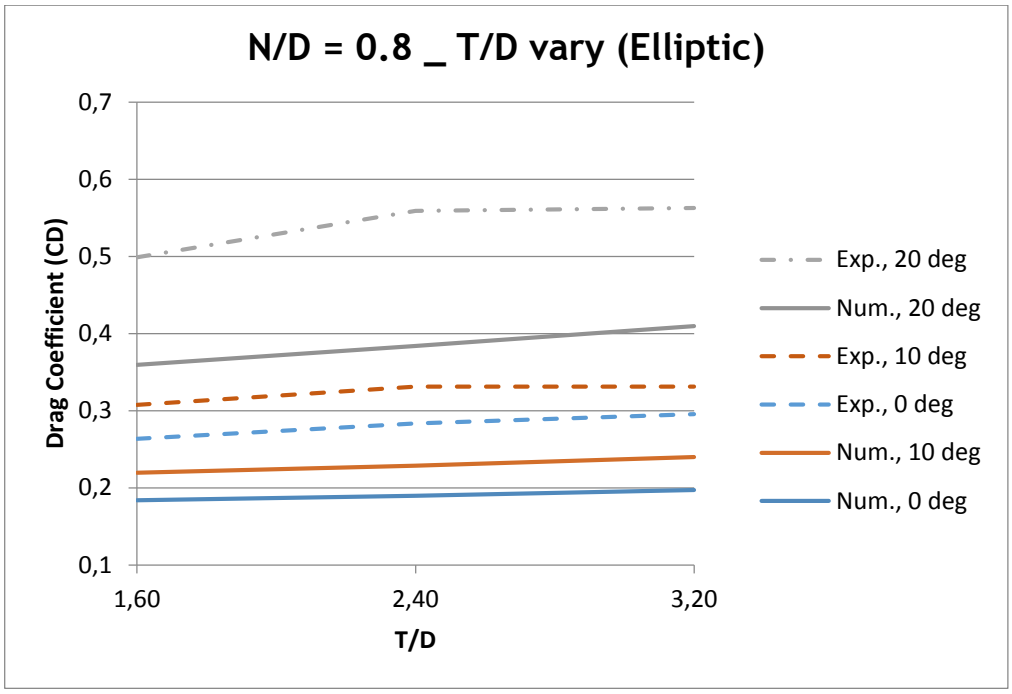

Chart 5.2 - Comparison of C_D Results between Numerical and Experimental Procedure varying T/D ratio between 1.6 to 3.2 for an Elliptical Tail shape case.

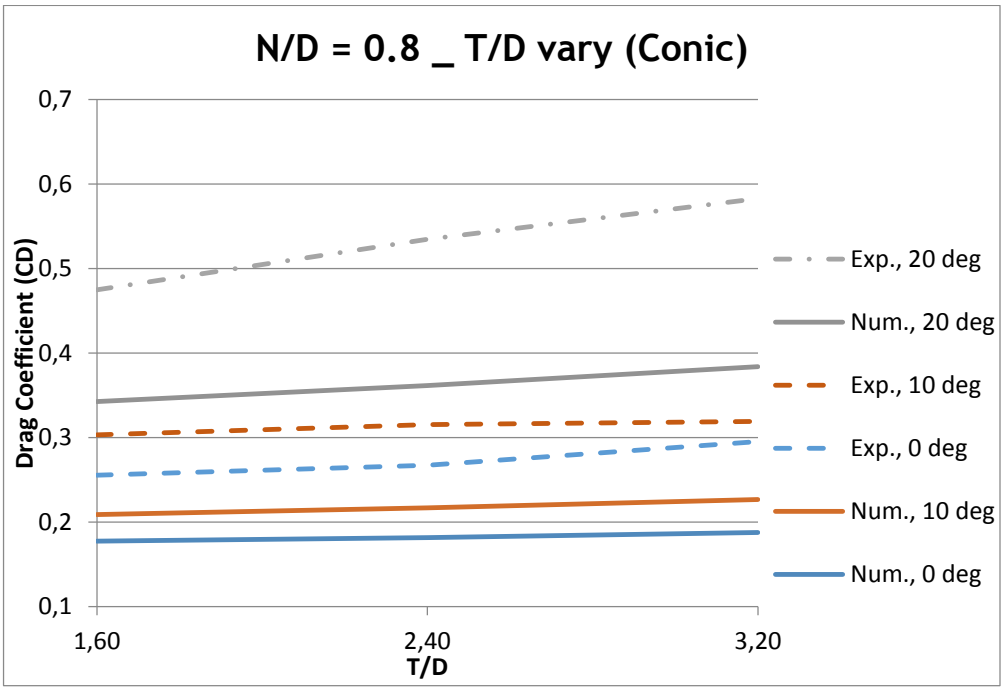

Chart 5.3 - Comparison of C_D Results between Numerical and Experimental Procedure varying T/D ratio between 1.6 to 3.2 for a Conical Tail shape case.

As can be seen in Chart 5.2 & Chart 5.3, Drag's behavior between them is similar. Moreover, the Drag's behavior between Experimental and Numerical Results is also similar, although there

is an offset between them. The deviation for each T/D ratio between Experimental and Numerical Results is observed at Table 5.4, for Elliptical and Conical cases.

Table 5.4 – Error % between Exp. & Num. Results (Elliptical & Conical Tails, respectively).

T/D	AOA	%ERROR
1.6	0	30
1.6	10	29
1.6	20	28
2.4	0	33
2.4	10	31
2.4	20	31
3.2	0	33
3.2	10	28
3.2	20	27

T/D	AOA	%ERROR
1.6	0	31
1.6	10	31
1.6	20	28
2.4	0	32
2.4	10	31
2.4	20	32
3.2	0	36
3.2	10	29
3.2	20	34

Table 5.4 demonstrates a difference between 27% to 36%, when comparing Experimental and Numerical Results, for both Tail shapes. Since there are several errors associated with this Comparison (Error scale effect, Reynold's number similarity, Towing tank conditions, Load cell precision, Numerical predictions and even water's temperature) these results indicate a good agreement.

The Chart 5.2 & Chart 5.3 also concludes that the Conical Tail produces a lower Drag for Experimental and Numerical Results. This phenomenon can be understood by visually analyzing the Figure 5.4.

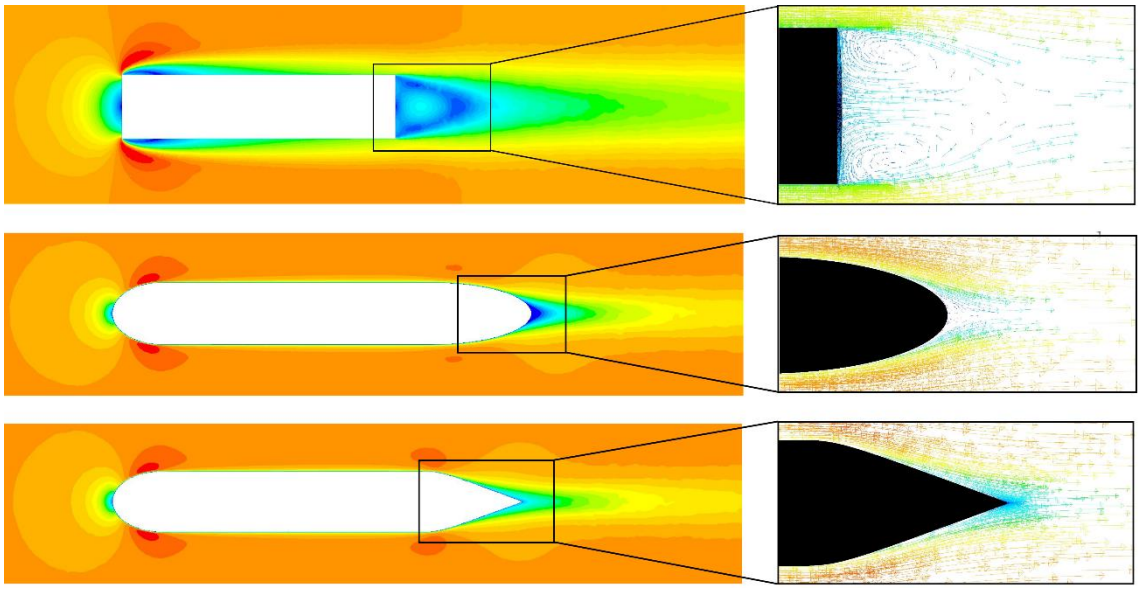

Figure 5.4 - Velocity contours/vectors for different Tail configurations at nominal velocity (full-scale prototype) of 0.45 m/s.

The Figure 5.4 shows different Tail configurations operating at 0° of AoA and nominal velocity of 0.45 m/s for full-scale prototype, and their associated velocity phenomena. Thus, by analyzing the Figure 5.4 and following the energy conservation principle, it can be seen that the Conical Tail produce a lower Drag when compared with the other geometries. The first line of Figure 5.4, shows a hull body without nose and tail, where the velocity achieves its lowest point at Nose or Bow, since there is no Nose in this case. This point is known as Stagnation Point (following the energy conservation principle, this point is also the highest point of pressure). At Tail or Stern, there are several Eddies created (Large and Small Scale). These Eddies, contribute greatly to the increase of Drag, becoming smaller with an Elliptical Tail (Figure 5.4 - second line) and almost disappearing with Conical Tail (Figure 5.4 – third line). Therefore, Figure 5.4 also validates the Conical Tail as being the configuration that produces the lowest Drag (according to the geometries observed on this study). The size of eddies (length scale) is highest for geometries without nose and tail, decreasing for elliptical geometries and achieve its lowest size for conical geometries. Moreover, Drag decreases with the decrease of size.

Chapter 6

6 Conclusions

An experimental procedure has been developed to investigate the effects of velocity, angles of attack and length-to-diameter ratio on the forces and coefficients acting on a torpedo-shaped hull body travelling at fully submerged depth. Using the commercial software ANSYS FLUENT, numerical simulations have been completed to validate them against experimental results.

At the beginning of this study, the objectives consisted in a hydrodynamic optimization, by Experimental Tests and Numerical Simulation, of a single-hull vehicle with similar dimensions of MEDUSA Deep-Sea lower-hull. However, due to several restrictions, the hull's dimensions were adapted to make this study possible. Thus, these dimensions leaded to a need of a Reynold's Number Similarity between full scale prototype and smaller hull prototype to predict hydrodynamic forces and coefficients.

6.1 Difficulties

Although the aim of this study was the validation of the Numerical Simulation with the Experimental Procedure, the Experimental Setup was, undoubtedly, the phase in which most issues occurred. The Experimental Setup process was, at the same time, very challenging and enriching. This process was not considered at the beginning, however, due to its necessity, it was also implemented. A lot of issues requiring a lot of time/efforts spent were encountered. Many considerations and procedures were adopted to overcome all of these complications. Nevertheless, some of these issues were not possible to overcome, like the lack of a dynamometer (load cell) applied for lower tensions or the rail offset (relatively to towing tank). Several rails corrections were made, albeit with no success due to material deformity. The solution adopted to avoid this problem was to find a location inside the towing tank, in which the results were not affected by rail offset. Regarding to the dynamometer, several options were attempted, like using load cells of a conventional balance weight or using a load cell (20kgs) with a MSP430 micro-CPU (Central Processing Unit), however these options were not well succeeded.

Finding a functional thread to pull the towing carriage was also very challenging. The requirements initially imposed were to find a thread with a low diameter that can be neglected (higher diameters could introduce low pitch angles on towing carriage when the thread was rolling) and that was able to hold relatively high tension forces (the tension necessary to start pulling the towing carriage was up to twenty times more than the tensions observed and considered on this study). To avoid these tensions, the Frequency Inverter was programmed to

have a slope at the Start/End of each run, i.e. during each run, the towing carriage started gradually to increase its velocity until reached the desired speed and the opposite happened at the end. The returning process used was extremely hard to implement, due to the necessity of leaving a precise clearance at the returning thread to do not interfere on results. However, once implemented, it was possible to fully control the towing carriage only with the Frequency Inverter.

The Model Design/Prototype Manufacturing was also a challenging process. Although, as could have been anticipated, the Prototype Manufacturing was made by a commercial company, leading to a number of restrictions imposed to the Model Design. This has led to continue monitoring by a professional CAD designer to fully respect imposed restrictions. The AoA system was a helpful method created to exactly respect the desired pitch angle. Many interactions between the Design and the Production of the prototype were observed and learned during this process.

Regarding the results obtained from the Experimental Procedure, these seems acceptable. Initially, it was expected to predict clearly the hydrodynamic forces and coefficients for each specific combination, although with the conditions imposed by materials that were being used, finishing all the Experiments was not possible. However, the data collected was more than sufficient to later validate against the Numerical Simulation. Before data analyzing, and after in some cases, the Experiment Test Results were not coherent, demonstrating the influence caused by several problems (as referred above). Nevertheless, as every Experimental Procedure, many lessons were learned during this process. It was concluded that the temperature of the water used on the towing tank was a crucial parameter to this study (greatly affecting the Reynolds number used for the Reynold's similarity by varying the Density and Viscosity). However, this parameter was not controllable by author. During a day, the water's temperature could vary, depending on the laboratory's temperature.

The Numerical Simulations were fully dependent to the computational time cost, leading to, in some cases, some simulations longing for several days. Find an acceptable range of y^+ was also very challenging.

6.2 Results

The small dimensions of the towing tank directly interfered with Results, showing better Results for smaller geometries. However, by the Numerical Study made, this is not always true. Thus, as proven by Figure 5.4, too small geometries produce higher Drag (influence of Eddies at Stern).

Analyzing the geometries studied for Experimental and Numerical Studies, the Elliptical and Conical Tail shape showed similar Results for both studies, although the Conical Tail shape demonstrated to be the optimum configuration, producing the lowest Drag.

Relatively to the Experimental Results, N/D = 0.8 and T/D = 1.6 was the optimum configuration. Although there are some questionable results for high AoA's and velocities, especially for 20° of AoA and traveling at 1 m/s. However, these Results are quite interesting to note, once there is a lack of Towing Tank studies varying AoA's. Normally, studies made by other authors [52], observe the effect of submergence depth, velocity or sideslip angle. Results demonstrate that AoA's greater than 20° should be avoided for further Towing Tank tests.

The Numerical Simulation was validated against the Experimental Tests, demonstrating a percentage Error between 27 and 36 %. This error difference could be optimized depending on CPU costs or using a more precise equipment on experimental procedure. However, the Standard κ-ε Turbulence model showed a good prediction for Drag values using low computational costs, when compared with other Turbulence Models (as κ-ω SST Model). Simulations also support the Experimental Tests Results on the optimum configuration, predicting the Conical Tail has the configuration that produces a lower Drag. Furthermore, these Simulations also revealed a huge increase on Drag for higher AoA's (20°), denoting that operation under high AoA's should be avoid.

It can be concluded that, the Results, in general, showed a good and adequate agreement. Although, several considerations/methods can be adopted to improve Experimental and Numerical Results. Some of these considerations are going to be described in next section (Further Works).

6.3 Further Work

As mentioned throughout this thesis, there are several considerations that were not accounted, due to lack of some resources/equipment. Therefore, results can be improved by solving some of these mishaps or finding alternative solutions for them. Further Work is here purpose to improve the results or to expand this study. These further work topics are:

- A Particle Image Velocimetry (PIV) system should be used to precisely analyze the flow around the hull body. The phenomena observed could then be compared with Numerical Simulations to guarantee similar behavior of flow between Numerical and Experimental procedures;
- Using other Towing Tank (higher dimensions) and a more precise Dynamometer, the Tests should be repeated and other parameters can be also tested, as Sideslip angle;
- Through other Turbulence Models (higher CPU cost), evaluate the difference of Results, justifying precisely the trade-off between Quality of Results/Computational Costs;

- A complete study using ASE methods should be done for Experimental correction. Thus, the error associated for each case (considering the error of each component) should be determined;
- A study of fairing's influence should be done. This study must comprise results for tests with and without fairings to evaluate its necessity;
- A similar study should be done using a hull body with appendages to compare both cases. Drag should be measured, firstly, for hull body and then including all components.

Bibliography

[1] "Woods Hole Oceanographic Institution." [Online]. Available: http://www.whoi.edu/. [Accessed: 05-Oct-2016].

[2] L. A. LA Gonzalez, "Design , Modelling and Control of an Autonomous Underwater Vehicle," *BE Thesis, Univ. West. Aust.*, p. 156, 2004.

[3] A. U. K. Carjova, P. Vulans, and I. Ozols, "Analysis of Buoyancy and Design Features of the Underwater Vehicle," pp. 327–334, 2012.

[4] N. A. Cruz, *Autonomous Underwater Vehicles*. 2011.

[5] J. Paulo and S. Morgado, "Persistent Gliding Waterframe The Waterframe Conceptual Project," no. June, 2011.

[6] P. E. Hagen, Ø. Hegrenæs, B. Jalving, Ø. Midtgaard, M. Wiig, and O. K. Hagen, "Making AUVs Truly Autonomous," no. December, 2008.

[7] P. Ridley, J. Fontan, and P. Corke, "Submarine Dynamic Modeling," *Proceeding 2003 Australas. Conf. Robot. Autom.*, pp. 1–3, 2003.

[8] J. Lucas, D. Dantas, E. A. De Barros, F. A. Mutscheler, and C. H. Umeda, "Experimental Research on Auv Manoeuvrability," no. 2009, 2011.

[9] R. B. Wynn, V. A. I. Huvenne, T. P. Le Bas, B. J. Murton, D. P. Connelly, B. J. Bett, H. A. Ruhl, K. J. Morris, J. Peakall, D. R. Parsons, E. J. Sumner, S. E. Darby, R. M. Dorrell, and J. E. Hunt, "Autonomous Underwater Vehicles (AUVs): Their past, present and future contributions to the advancement of marine geoscience," *Mar. Geol.*, vol. 352, pp. 451–468, 2014.

[10] A. Palmer, G. E. Hearn, and P. Stevenson, "Experimental Testing of an Autonomous Underwater Vehicle with Tunnel Thrusters," *First Int. Symp. Mar. Propuls.*, no. June, pp. 1–6, 2009.

[11] J. L. D. Dantas and E. A. de Barros, "Numerical analysis of control surface effects on AUV manoeuvrability," *Appl. Ocean Res.*, vol. 42, pp. 168–181, 2013.

[12] "MEDUSA Deep-Sea," 2016. [Online]. Available: www.medusadeepsea.com. [Accessed: 05-Oct-2016].

[13] G. Kirby, "the Development of Rocket-Propelled Torpedoes," pp. 1–15, 2000.

[14] S. K. Jain, S. Mohammad, S. Bora, and M. Singh, "A Review Paper on: Autonomous Underwater Vehicle," vol. 6, no. 2, pp. 38–40, 2015.

[15] R. Krishnan, "Introduction to," *Control*, no. 1, 1989.

[16] C. Von Alt, "Autonomous underwater vehicles," *Auton. Underw. Lagrangian Platforms …*, pp. 1–5, 2003.

[17] D. R. Blidberg, "The development of autonomous underwater vehicles (auvs); a brief summary," *Ieee Icra*, vol. 6500, 2010.

[18] H. R. Widditsch, "SPURV-The First Decade," *APL-UW 7215, Appl. Phys. Lab. Univ. Washingt.*, p. 32, 1973.

[19] "Bluefin Robotics AUV's » Bluefin Robotics." [Online]. Available:

http://www.bluefinrobotics.com/. [Accessed: 06-Sep-2016].

[20] "The HUGIN Family : Maximizing performance," 2010.

[21] K. Simrad and K. Simrad, "The Autonomous Underwater Vehicle (AUV): A Cost-Effective Alternative to Deep-Towed Technology," pp. 65–69, 1995.

[22] "Kongsberg Maritime AUV product line : Maximizing performance by providing."

[23] T. H. E. Arts, C. Policy, C. Justice, N. Security, P. Safety, and H. Security, *The RAND Corporation is a nonprofit research Support RAND Purchase this document Make a charitable contribution For More Information Visit RAND at www.rand.org*. 2010.

[24] M. Moonesun and Y. Mikhailovich, "Minimum immersion depth for eliminating free surface effect on submerged submarine resistance," *Turkish J. Eng. , Sci. Technol.*, vol. 1, pp. 36–46, 2015.

[25] E. Dawson, "An Investigation into the Effects of Submergence Depth , Speed and Hull Length-to-Diameter Ratio on the Near- Surface Operation of Conventional Submarines," no. November, 2014.

[26] M. S. Triantafyllou and F. S. Hover, "Maneuvering and Control of Marine Vehicles," 2003.

[27] C. H. Wolowicz, J. S. Bowman-Jr, and W. P. Gilbert, "Similitude requirements and scaling relationships as applied to model testing," *NASA Tech. Pap. 1435*, no. August, pp. 1–61, 1979.

[28] L. Larsson and H. Raven, *The Principles of Naval Architecture Series: Ship Resistance and Flow*. 2010.

[29] V. Bertram, *Practical Ship Hydrodynamics*. 2000.

[30] P. P. N. Joubert, "Some Aspects of Submarine Design Part 2 . Shape of a Submarine 2026," *Design*, 1920.

[31] P. P. N. Joubert, "Some Aspects of Submarine Design Part 1 . Hydrodynamics," *Dep. Defence, Aust. Goverment*, 2004.

[32] D. H. Schlichting and K. Gersten, "Boundary-layer theory," *Eur. J. Mech. - B/Fluids*, vol. 20, p. 817, 1979.

[33] J. Southard, "Flow Past a Sphere II: Stoke's Law, the Bernoulli Equation, Turbulence, Boundary Layers, Flow Seperation," *Spec. Top. An Introd. to Fluid Motions, Sediment Transp. Curr. Sediment. Struct. (Lecture Notes)*, pp. 35–82, 2006.

[34] P. C. Praveen and P. Krishnankutty, "Study on the effect of body length on the hydrodynamic performance of an axi-symmetric underwater vehicle," vol. 42, no. December, pp. 1013–1022, 2013.

[35] M. Moonesun, M. Javadi, P. Charmdooz, and K. U. Mikhailovich, "Evaluation of submarine model test in towing tank and comparison with CFD and experimental formulas for fully submerged resistance," *Indian J. Mar. Sci.*, vol. 42, no. 8, pp. 1049–1056, 2013.

[36] K. Alam, T. Ray, and S. G. Anavatti, "Design and construction of an autonomous underwater vehicle," *Neurocomputing*, vol. 142, pp. 16–29, 2014.

[37] H. Kim, J. Moss, and C. R., “Research in Resistance and Propulsion,” 1963.

[38] ITTC, “ITTC – Recommended Procedures Testing and Extrapolation Methods Resistance Test,” *Int. Towing Tank Conf.*, p. 11, 2002.

[39] M. Renewables and I. Network, “Review of Tow Tank Limitations,” 2014.

[40] K. Tamura, “Study on the blockage correction,” *J. Soc. Nav. Archit. Japan*, vol. 17, no. 131, pp. 17–28, 1972.

[41] W. H. Mason, “8. Introduction to Computational Fluid Dynamics,” *Univ. Vermont Phys. J.*, pp. 1–46, 1998.

[42] “ANSYS Fluent Theory Guide,” vol. 15317, no. November, pp. 724–746, 2013.

[43] J. Katz and A. Plotkin, “Low Speed Aerodynamics,” *McGrawhill Inc*, no. February 2013, p. 351, 1991.

[44] J. Katz and A. Plotkin, *Low-Speed Aerodynamics*. 1991.

[45] W. H. Mason, “2 . Getting Ready for Computational Aerodynamics : Fluid Mechanics Foundations,” *Appl. Comput. Aerodyn.*, pp. 1–39, 1998.

[46] D. P. Brandão, “Development of a Framework for Static Aeroelastic Analysis of Flexible Wings including Viscous Flow Effects,” no. December, 2015.

[47] I. Most and T. To, “Essay 11 The RANS Equations The Basis of Turbulence Modeling,” *Test*, no. Ldv, pp. 1–5.

[48] T. Model, T. S. Model, T. Standard, S. Transport, T. Reynolds, S. Model, T. Large, E. Simulation, N. Treatments, W. T. Flows, G. Considerations, T. F. Simulations, P. Setup, T. Flows, and S. Strategies, “Chapter 10. Modeling Turbulence,” *Strategies*, pp. 1–102, 2001.

[49] “Reynolds-Averaged Navier-Stokes Equations | Symscape.” [Online]. Available: http://www.symscape.com/reynolds-averaged-navier-stokes-equations. [Accessed: 05-Oct-2016].

[50] I. FLUENT, “Modeling Turbulent Flows,” *ANSYS.Inc.*, pp. 6–2, 6–49, 2006.

[51] V. de Brederode, *Fundamentos de Aerodinâmica Incompressível*. 1997.

[52] S. Mansoorzadeh and E. Javanmard, “An investigation of free surface effects on drag and lift coefficients of an autonomous underwater vehicle (AUV) using computational and experimental fluid dynamics methods,” *J. Fluids Struct.*, vol. 51, pp. 161–171, 2014.

[53] “The small Maya AUV – Initial field results The small AUV Maya : Initial Field Results,” no. January 2007, 2016.

[54] E. A. De Barros, J. L. D. Dantas, A. M. Pascoal, and E. De Sá, “Investigation of normal force and moment coefficients for an AUV at nonlinear angle of attack and sideslip range,” *IEEE J. Ocean. Eng.*, vol. 33, no. 4, pp. 538–549, 2008.

[55] P. Jagadeesh and K. Murali, “Application of low-Reynolds turbulence models for flow simulations past undferwater vehicle hull forms,” *J. Nav. Archit. Mar. Eng.*, pp. 41–54, 2005.

[56] P. Jagadeesh, K. Murali, and V. G. Idichandy, “Experimental investigation of

hydrodynamic force coefficients over AUV hull form," *Ocean Eng.*, vol. 36, no. 1, pp. 113–118, 2009.

[57] K. Alam, T. Ray, and S. G. Anavatti, "A Study on the Drag Estimation of an AUV Based on Numerical Methods," pp. 1–6, 2012.

[58] C. Kunz, C. Murphy, R. Camilli, H. Singh, J. Bailey, R. Eustice, M. Jakuba, K. I. Nakamura, C. Roman, T. Sato, R. A. Sohn, and C. Willis, "Deep sea underwater robotic exploration in the ice-covered arctic ocean with AUVs," *2008 IEEE/RSJ Int. Conf. Intell. Robot. Syst. IROS*, pp. 3654–3660, 2008.

[59] "CATIA PLM Software Solution by Dassault Systèmes." [Online]. Available: http://www.3ds.com/products-services/catia/. [Accessed: 05-Oct-2016].

[60] ITTC, "Guidelines for uncertainty analysis in resistance towing tank tests," *25th Int. Towing Tank Comm.*, 2008.

[61] "Local Cells and Transducers, Industrial Sensors - AEP | Design and production of load cells." [Online]. Available: http://www.aeptransducers.com/. [Accessed: 05-Oct-2016].

[62] "Archimedes Principle Formula | Formulas@TutorVista.com." [Online]. Available: http://formulas.tutorvista.com/physics/archimedes-principle-formula.html. [Accessed: 05-Oct-2016].

[63] L. Wu, Y. Li, S. Su, P. Yan, and Y. Qin, "Hydrodynamic analysis of AUV underwater docking with a cone-shaped dock under ocean currents," *Ocean Eng.*, vol. 85, pp. 110–126, 2014.

[64] A. Release, "Meshing Help," *Portal*, vol. 15317, no. January, pp. 724–746, 2007.

Appendix A

A Images of final Experimental Model

A.1 Experimental Prototype Configuration

Figure A.1 – Full Prototype Configuration after manufacturing; Here, it can be seen the hull body at 20° of AoA during testing stages.

A.2 Prototype Nose and Tail configurations

Figure A.2 – Nose and Tail configurations; Here, it can be seen several Nose/Tail configurations used on Experimental Tests.

Appendix B

B Images of the real Experimental layout

B.1 Image of Towing Tank length

Figure B.1 – Towing tank without water; Here, it can be also seen a first unsuccessful mount configuration with a different motor.

B.2 Image of the hull body on Towing Tank

Figure B.2 – Model's attitude travelling at 20˚; Here, it can be seen the hull body at the starting position.

Appendix C

C Images of Experimental Setup (Processes)

C.1 Early phase

Figure C.1 – Initial Experimental Setup; As can be seen, a different motor and tube were also tested.

C.2 Dynamometer

Figure C.2 – Initial Dynamometer used; Here, it can be also seen the tubes where the water entered on the Towing Tank.

C.3 Returning System

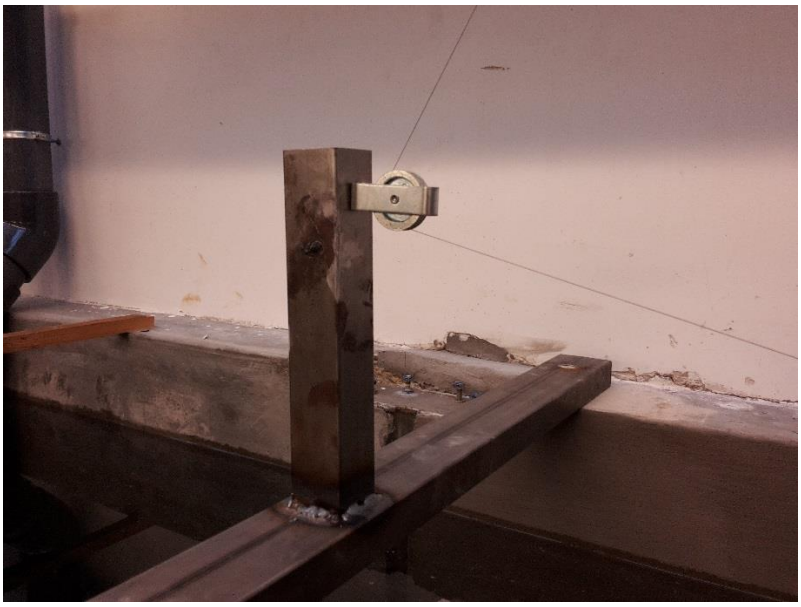

Figure C.3 – System added to the Towing Tank for an autonomous returning.

C.4 Thread System used for the Returning System

Figure C.4 – Thread System used; the supporting blue thread was used to guarantee a safe distance between the pulling/pushing thread.

C.5 Final Experimental Setup

Figure C.5 – Experimental System used during Experiments; Several attempts/considerations were made to achieve this Setup.

Appendix D

D Images of Control and Data Collection

D.1 Frequency Inverter

Figure D.1 – Frequency Inverter used; Here, it can be seen a pre-programmed run for 13 Hz (0.75 m/s).

D.2 WiMOD Device & Load Cell

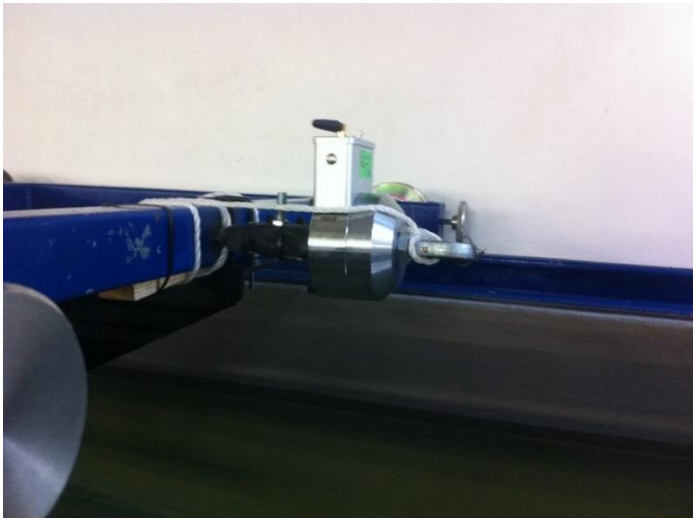

Figure D.2 – System used to measure the Towing Carriage Drag; Here, it can be seen an attached device to the Load Cell to communicate (wireless) with the Receiver Device. A safe system was made to guarantee material's safety.

D.3 WiSTAR Device

Figure D.3 – WiSTAR Device used to receive Data via Wireless.

Appendix E

E Weight difference consideration

E.1 Weights used

Figure E.1 – Weights used for Experimental Tests (range of 50 to 3000 g).

E.2 Fixing Weights

Figure E.2 – Towing Carriage with Weights; Here, it can be seen that depending on hull's AoA, the Weights position changes.

Appendix F

F Data analysis

F.1 Data analysis layout

Table F.1 – Parameters considered for each case; Here, as can be seen, several parameters were calculated; For each case, 10 runs were made. However, these 10 runs are omitted here (only final values are shown).

Tests	N/D	T/D	Area	Rn	Velocidade	Pitch angle	Combination	devpad	New average	Uncertainty in the Mean	Measured Value	Uncertainty (%)	Final Drag(Body)
4	0.8	1.6	0.123	4.70E+05	0.50	0	E1N-C1T	0.28	3.53	0.086	3,54+-0,09	2.4	0.45
5	0.8	2.4	0.134	4.70E+05	0.50	0	E1N-C2T	0.55	3.59	0.163	3,6+-0,17	4.5	0.50
6	0.8	3.2	0.145	4.70E+05	0.50	0	E1N-C3T	0.55	3.68	0.133	3,68+-0,14	3.6	0.59
24	0.8	1.6	0.123	4.70E+05	0.50	10	E1N-C1T	0.31	3.99	0.145	4+-0,15	3.6	0.52
25	0.8	2.4	0.134	4.70E+05	0.50	10	E1N-C2T	0.28	4.07	0.112	4,07+-0,12	2.7	0.60
26	0.8	3.2	0.145	4.70E+05	0.50	10	E1N-C3T	0.36	4.14	0.138	4,14+-0,14	3.3	0.67
44	0.8	1.6	0.123	4.70E+05	0.50	20	E1N-C1T	0.52	4.24	0.000	4,24+-0	0.0	0.73
45	0.8	2.4	0.134	4.70E+05	0.50	20	E1N-C2T	0.55	4.31	0.000	4,31+-0	0.0	0.81
46	0.8	3.2	0.145	4.70E+05	0.50	20	E1N-C3T	0.49	4.34	0.164	4,34+-0,17	3.8	0.83
64	0.8	1.6	0.123	7.04E+05	0.75	0	E1N-C1T	0.30	4.63	0.151	4,63+-0,16	3.3	0.53

Tests	N/D	T/D	Area	Rn	Velocidade	Pitch angle	Combination	devpad	New average	Uncertainty in the Mean	Measured Value	Uncertainty (%)	Final Drag(Body)
65	0.8	2.4	0.134	7.04E+05	0.75	0	E1N-C2T	0.50	4.68	0.145	4,68+-0,15	3.1	0.58
66	0.8	3.2	0.145	7.04E+05	0.75	0	E1N-C3T	0.93	4.72	0.255	4,73+-0,26	5.4	0.63
84	0.8	1.6	0.123	7.04E+05	0.75	10	E1N-C1T	0.50	5.01	0.189	5,02+-0,19	3.8	0.60
85	0.8	2.4	0.134	7.04E+05	0.75	10	E1N-C2T	0.98	5.05	0.187	5,05+-0,19	3.7	0.64
86	0.8	3.2	0.145	7.04E+05	0.75	10	E1N-C3T	0.46	5.10	0.138	5,11+-0,14	2.7	0.69
104	0.8	1.6	0.123	7.04E+05	0.75	20	E1N-C1T	0.49	5.07	0.217	5,07+-0,22	4.3	0.88
105	0.8	2.4	0.134	7.04E+05	0.75	20	E1N-C2T	1.06	5.11	0.296	5,11+-0,3	5.8	0.92
106	0.8	3.2	0.145	7.04E+05	0.75	20	E1N-C3T	0.83	5.15	0.232	5,16+-0,24	4.5	0.96
124	0.8	1.6	0.123	9.39E+05	1.00	0	E1N-C1T	0.63	5.05	0.212	5,06+-0,22	4.2	0.64
125	0.8	2.4	0.134	9.39E+05	1.00	0	E1N-C2T	0.44	5.08	0.117	5,08+-0,12	2.3	0.67
126	0.8	3.2	0.145	9.39E+05	1.00	0	E1N-C3T	0.82	5.15	0.207	5,15+-0,21	4.0	0.74
144	0.8	1.6	0.123	9.39E+05	1.00	10	E1N-C1T	0.69	5.45	0.189	5,45+-0,19	3.5	0.76
145	0.8	2.4	0.134	9.39E+05	1.00	10	E1N-C2T	0.64	5.47	0.159	5,47+-0,16	2.9	0.79
146	0.8	3.2	0.145	9.39E+05	1.00	10	E1N-C3T	0.64	5.48	0.177	5,49+-0,18	3.2	0.80
164	0.8	1.6	0.123	9.39E+05	1.00	20	E1N-C1T	1.05	5.89	0.336	5,9+-0,34	5.7	1.19
165	0.8	2.4	0.134	9.39E+05	1.00	20	E1N-C2T	0.40	6.04	0.170	6,04+-0,17	2.8	1.34
166	0.8	3.2	0.145	9.39E+05	1.00	20	E1N-C3T	0.68	6.17	0.214	6,17+-0,22	3.5	1.46

F.2 Data collection

Table F.2 – Data collected for one Drag value; Here, each column represents data collected for one run. After 10 runs, the average value and the standard deviation were calculated; consecutively, the undesired values were excluded through data refinement (using the average value and the standard deviation).

Velocity - 0,5 m/s - 0 degrees										
Time[s]	**Drag [N]**									
0	0.000	0.000	0.000	0.000	0.000	0.000	0.000	0.000	0.000	0.000
1	0.000	0.000	-2.942	0.000	0.000	0.000	0.000	0.000	-1.961	0.000
2	0.000	-19.613	-2.942	0.000	-2.942	-2.942	-4.903	-1.961	-1.961	-1.961
3	0.000	-13.729	-23.536	-43.149	-2.942	-2.942	-3.923	-1.961	-45.111	-50.995
4	-14.710	-15.691	-20.594	-20.594	-28.439	-25.497	-27.459	-19.613	-16.671	-2.942
5	-13.729	-14.710	-16.671	-17.652	-25.497	-22.555	-23.536	-16.671	-14.710	-12.749
6	-12.749	-13.729	-11.768	-13.729	-20.594	-16.671	-18.633	-14.710	-12.749	-10.787
7	-8.826	-11.768	-8.826	-9.807	-15.691	-10.787	-13.729	-10.787	-8.826	-8.826
8	-7.845	-8.826	-5.884	-7.845	-8.826	-7.845	-8.826	-7.845	-7.845	-6.865
9	-4.903	-4.903	-4.903	-4.903	-7.845	-5.884	-4.903	-5.884	-5.884	-4.903
10	-4.903	-4.903	-4.903	-4.903	-4.903	-4.903	-4.903	-4.903	-4.903	-4.903
11	-4.903	-4.903	-4.903	-3.923	-4.903	-4.903	-3.923	-4.903	-3.923	-3.923

12	-3.923	-3.923	-3.923	-3.923	-3.923	-3.923	-3.923	-3.923	-3.923	-3.923
13	-3.923	-3.923	-3.923	-2.942	-3.923	-3.923	-3.923	-3.923	-3.923	-2.942
14	-2.942	-2.942	-2.942	-2.942	-3.923	-2.942	-2.942	-2.942	-3.923	-2.942
15	-2.942	-2.942	-2.942	-2.942	-2.942	-2.942	-2.942	-2.942	-2.942	-2.942
16	-2.942	-2.942	-2.942	-2.942	-2.942	-2.942	-2.942	-2.942	-2.942	-2.942
17	-2.942	-2.942	-1.961	-2.942	-2.942	-2.942	-2.942	-2.942	-2.942	-2.942
18	-1.961	-2.942	0.000	-0.981	-2.942	-1.961	-1.961	-2.942	-1.961	-0.981
19	0.000	-0.981	0.000	0.000	-1.961	0.000	-0.981	-0.981	-0.981	0.000
20	0.000	0.000	0.000	0.000	0.000	0.000	0.000	0.000	0.000	0.000
Average	**-4.483**	**-6.49105**	**-6.02405**	**-6.95805**	**-7.05143**	**-6.024**	**-6.53781**	**-5.37024**	**-7.05148**	**-6.11752**